Engineering Geology 343 (2024) 107776

Contents lists available at ScienceDirect

Engineering Geology

journal homepage: www.elsevier.com/locate/enggeo

Environmental effects and ESI-07 intensity of the M_w 7.7, September 19th, 2022, Michoacán, Mexico, earthquake

María Magdalena Velázquez-Bucio [a,*], Maria Francesca Ferrario [b], Pierre Lacan [a], Eliana Muccignato [b], Marco Pizza [b], Aaditya Sridharan [c], Sabina Porfido [d,e], Sundararaman Gopalan [f], Andrés Nuñez-Meneses [g], Alessandro Maria Michetti [b,e]

[a] Instituto de Geociencias, Universidad Nacional Autónoma de México, Blvd. Juriquilla, 3001, 76230 Juriquilla, Querétaro, Mexico
[b] Dipartimento di Scienza ed Alta Tecnologia, Università degli Studi dell'Insubria, Via Valleggio 11, 22100 Como, CO, Italy
[c] Department of Physics, Amrita Vishwa Vidyapeetham, Amritapuri, India
[d] CNR-ISA, Via Roma, 64, 83100 Avellino, AV, Italy
[e] Istituto Nazionale di Geofisica e Vulcanologia, Osservatorio Vesuviano, Via Diocleziano 328, 80124 Naples, Italy
[f] Department of Electronics and Communication Engineering, Amrita Vishwa Vidyapeetham, Amritapuri, India
[g] Posgrado en Ciencias de la Tierra, Instituto de Geociencias, Universidad Nacional Autónoma de México, Blvd. Juriquilla No. 3001, 76230 Juriquilla, Querétaro, Mexico

ARTICLE INFO

Keywords:
Earthquake Environmental Effects
ESI-07 scale
Seismic hazard
Subduction earthquakes
Michoacán Mexico 2022 earthquake

ABSTRACT

Most seismic risk assessments primarily focus on the impact of ground acceleration on infrastructure. However, in Mexico, along with numerous countries in Latin America and beyond, a significant portion of earthquake risk stems from secondary environmental effects such as tsunamis, landslides, and liquefaction processes. These secondary effects can often prove more lethal than the earthquake shaking itself. We used the Environmental Seismic Intensity scale (ESI-07) to assess the Earthquake Environmental Effects (EEEs) of the M_w 7.7 Michoacan earthquake on September 19th, 2022. This made it possible to comprehensively characterize the EEEs and their potential social consequences in the epicentral area along the Mexican subduction zone. Our study draws on data gathered from extensive field surveys, satellite imagery analysis, social media monitoring, and online resources, totalling data from over 8000 sites with EEEs. Through rigorous analysis, ESI-07 intensity values illuminate the vulnerability of coastal areas and coastal ranges to specific secondary effects triggered by large seismic events. We meticulously map the spatial distribution of these triggered EEEs, presenting A) an ESI-07 isoseismal map, and B) comparative analysis with other significant earthquakes, particularly subduction megathrust interface events. Our findings underscore the critical importance of considering environmental coseismic effects and using the ESI-07 scale in territorial planning and seismic risk preparedness. Furthermore, we highlight the unique characteristics of the Mexican Pacific coastal region and, more broadly, the distinct risks posed by coastal areas along subduction zones in terms of secondary seismic environmental hazards. This work emphasizes the urgent need to acknowledge the vulnerability of these regions to secondary effects and the imperative for resilience-building measures to safeguard human well-being and mitigate economic repercussions in the face of future seismic events.

1. Introduction

The Earthquake Environmental Effects (EEEs) testify to the profound impacts of seismic activity on the natural environment, encompassing primary effects like surface rupture, regional uplift or subsidence, and secondary hazards such as liquefaction or landslides (e.g., Serva et al., 2016; Ferrario et al., 2022; Hill et al., 2024). Recent major earthquakes around the world have underscored the substantial influence of these effects on affected regions and their societal repercussions (e. g., Bhattacharya et al., 2011; Verdugo and González, 2015; Fan et al., 2019; Imamura et al., 2019; Porfido et al., 2020; Papathanassiou et al., 2022; Wirth et al., 2022; Chen et al., 2023; Hill et al., 2024). The Environmental Seismic Intensity 2007 (ESI-07) scale, crafted by Michetti et al. (2007), systematically categorizes these effects. It is especially beneficial in sparsely populated areas where human and structural impacts may be challenging to document (e.g., Dengler and McPherson, 1993). It allows

* Corresponding author.
E-mail address: magda_vb@yahoo.com.mx (M.M. Velázquez-Bucio).

https://doi.org/10.1016/j.enggeo.2024.107776
Received 24 February 2024; Received in revised form 18 October 2024; Accepted 27 October 2024
Available online 3 November 2024

mapping the distribution of EEEs generated by large seismic events, providing a detailed database suitable for engineering geology applications (Guerrieri et al., 2015; Papathanassiou et al., 2017a, 2017b; King et al., 2018; Naik et al., 2023a, 2023b). The Mexican subduction zone is an interesting setting to apply the ESI-07 scale, as the population in the coastal areas is regularly affected by extensive primary and secondary effects of major earthquakes (Velázquez-Bucio et al., 2023a; Fig. 1, 2). In fact, the study of EEEs for evaluating seismic hazard in Mexico is an under-explored endeavor.

Historical seismic events in Mexico, like the January 3rd, 1920, Ms.

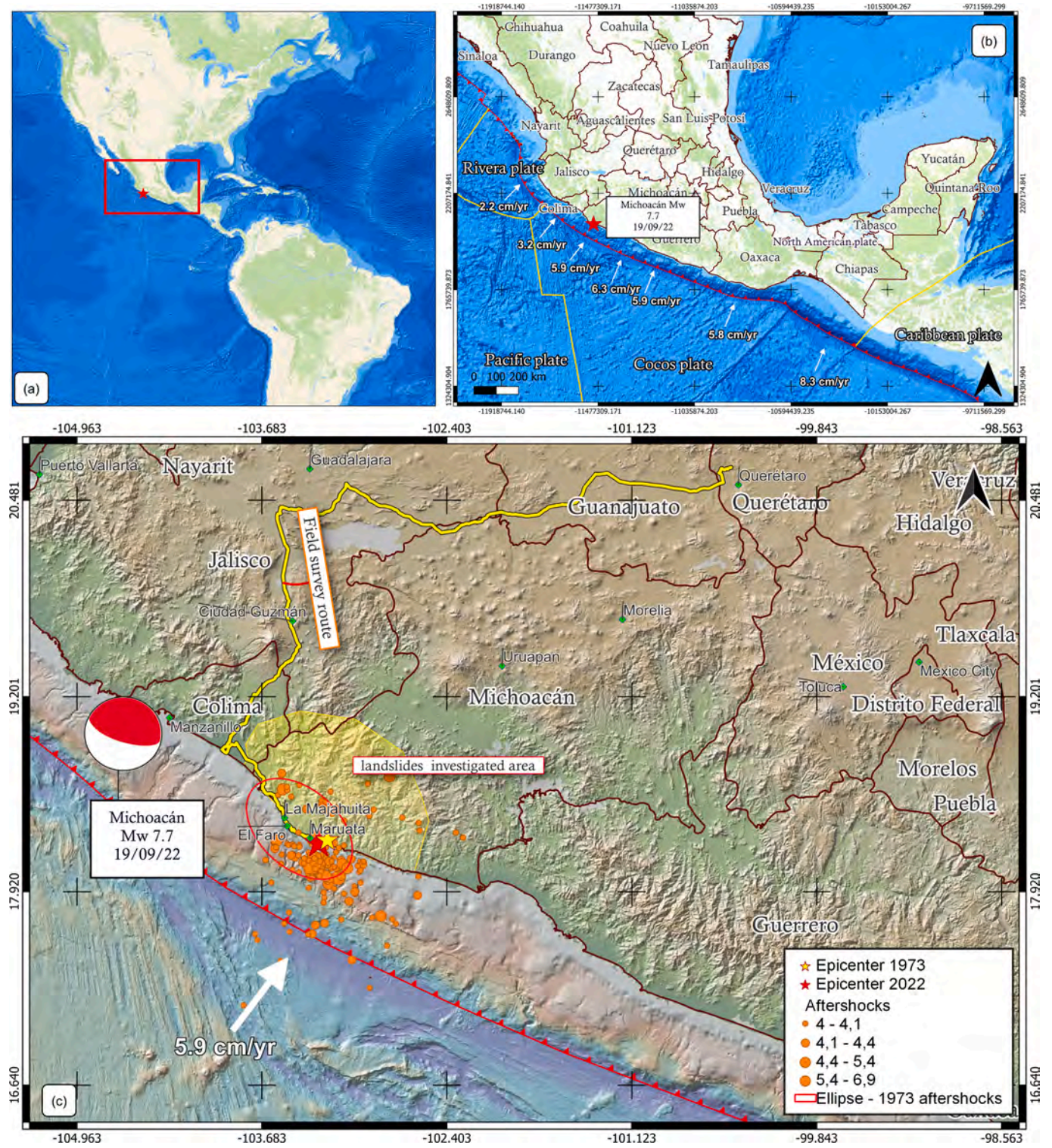

Fig. 1. (a, b) Geographic and geodynamic setting of the Mexican subduction zone and location of the study area; red star is the 2022 Michoacan mainshock. (c) Tectonic setting of the studied area, orange dots represent the $M_w \geq 4$ aftershocks registered by the SSN until December 13th, 2023; small yellow star and red ellipse shows respectively the epicenter, and the aftershocks area, of the January 30th, 1973, Mw 7.6 earthquake (Singh et al., 2023a; Liu et al., 2023); yellow line is the route taken during the two field campaigns from UNAM, Querétaro, to the epicentral area; yellow polygon outlines the landslides area analyzed from satellite imagery; basemaps provided by ©ESRI, plotted using ©GeoMapApp and ©ArcGISPro.

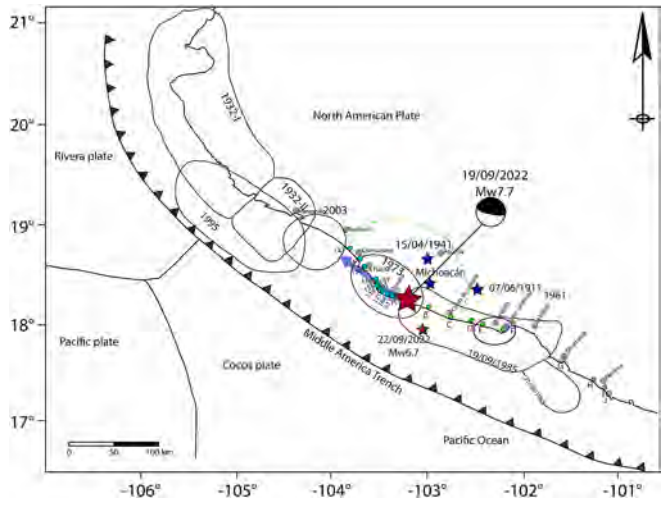

Fig. 2. Tectonic sketch map of the Mexican subduction zone, modified from Singh et al. (2023a) and Bodin and Klinger (1986); contours outline aftershock areas of large earthquakes; purple stars depict epicenters of the earthquakes whose aftershock areas are not known; red stars show epicenters of the 2022 mainshock (M_w 7.7) and the major aftershock (M_w 6.7); purple shadowed arrow indicates the direction of rupture propagation during the 2022 mainshock (Singh et al., 2023a); points in green (A-J) indicate the sites with a record of coastal uplift due to the 1985 earthquake (Bodin and Klinger, 1986), points in blue (the numbers indicate the ID for each site; see Table 1) are the sites with coastal uplift documented in our field work for the 2022 Michoacán earthquake; dashed green line outlines the area investigated (ca. 10,000 km^2) with satellite imagery for coseismic landslides, see detail in Fig. 9. (For interpretation of the references to color in this figure legend, the reader is referred to the web version of this article.)

6.2 (Mw 6.4) Xalapa earthquake (Suter et al., 1996; Suárez and Novelo-Casanova, 2018), demonstrate that seismically induced geological effects could cause more damage than ground shaking affecting structures. For instance, the environmental effects of the 1920 earthquake, such as landslides and debris flows, claimed more fatalities than the destruction by seismic shaking, highlighting the critical role of environmental effects in hazard assessment. Despite its relatively low magnitude, the 1920 event is the second deadliest seismic event in Mexican history after the 1985 Michoacan earthquake.

This work aims to assess the EEEs triggered by the M_w 7.7 Michoacan earthquake of September 19th, 2022, using the ESI-07 scale, thereby improving our understanding of the macroseismic intensity and behavior of the terrain specifically in a subduction zone setting. We adopted standard practice methods, with the added value of integrating three approaches; i) field reconnaissance, ii) collection of crowdsourced data from social media and online resources and iii) landslide mapping from satellite images. For this earthquake, we present more than 8000 sites with ESI-07 values, which are made publicly available (Velázquez-Bucio et al., 2023b). The number of sites is unprecedented since it is an order of magnitude higher with respect to all the other subduction earthquakes analyzed using the ESI-07 scale (Ferrario et al., 2022).

Macroseismology is an eminently observational and empirical science. For such data-driven approaches, the availability of more and more case studies from a variety of settings will result in more robust outcomes. The ESI-07 scale, ratified by INQUA (International Union for Quaternary Research), during the XVII INQUA Congress in 2007, is based on a global review of environmental effects from numerous major earthquakes, carried out by an international group of geologists, seismologists and engineers. Nevertheless, since this scale was released more recently than other available macroseismic scales, the number of earthquakes analyzed using this scale is still limited, and thus the analysis of new earthquakes is needed to increase the available data. Studies of this type are especially necessary, since the compilation carried out by Ferrario et al. (2022), demonstrates the effectiveness and importance of the ESI-07 scale to characterize the EEEs in various geodynamic contexts, evaluate attenuations in the epicentral zone, and consequently, improve the characterization of the associated hazard and risk.

Using the ESI-07 scale systematically not only helps in understanding macroseismic intensity, but also contributes to identifying engineering geology issues and environmental hazards for populations living in seismically-prone areas. In the following, we analyze the spatial distribution of the EEEs triggered by the 2022 Michoacán earthquake and present an ESI-07 isoseismal map. The evaluation of intensity through damage to man-made structures tends to reflect the economic and cultural development of the place (Serva et al., 2016). Unlike near real-time maps of ground motion and shaking intensity (e.g., Shakemaps), the ESI-07 scale offers an alternative perspective through direct field observations to categorize and evaluate both primary and secondary effects of an earthquake in natural settings. This approach captures aspects not fully grasped by intensity scales that deal largely with damage to the built environment. The ESI-07 scale comprises twelve degrees of intensity, each one related to the characteristics and dimensions of the considered EEEs. This scale does not aim to replace traditional intensity scales; in fact, by integrating the ESI-07 scale with those traditional scales, areas vulnerable to specific effects depending on the terrain, topography, and geological elements can be identified, which are fundamental aspects in territorial planning and infrastructure design. This makes it an additional useful tool for engineering geology in seismic risk assessment and disaster mitigation. We focus on the peculiarities of the Mexican coastal region and we explore how the analysis of EEEs may improve our understanding of seismic events, their implications for the natural environment, and their societal consequences.

2. Regional setting

2.1. Seismotectonics

Mexico is a region of high seismicity due to the differential movement between five tectonic plates: the North American, Caribbean, Cocos, Pacific, and Rivera plates (Fig. 1). The major seismic sources result from the convergence of the Rivera and Cocos plates below the North American Plate. The Cocos Plate records higher convergence rates, ranging from 3 to 7 cm/year (DeMets et al., 2010), increasing along strike from NW towards the Tehuantepec Ridge in the SE part of the Mexican subduction zone (DeMets et al., 1994; De Mets and Wilson, 1997; DeMets et al., 2010; Melgar et al., 2020). The Rivera Plate, comparatively smaller than the Cocos and North American plates, exhibits a slower convergence rate of 2.5 cm/year with respect to the North American Plate.

The subduction leads to both interface and intraslab seismicity in central and south-western Mexico, identified as the most seismically active regions in the country (Ordaz and Reyes, 1999; Zúñiga et al., 2017; Chen et al., 2018; Suárez et al., 2020). Specifically, the Jalisco-Colima-Michoacán segment, the area affected by the earthquake on September 19th, 2022, corresponds to a complex interaction between the Rivera, Cocos, North American, and Pacific plates (Singh and Pardo, 1993; Pardo and Suárez, 1995; DeMets et al., 1994, 2010; Sawires et al., 2021). Megathrust events along the plate interface typically taking place at 5–35 km depths in this setting (Suárez et al., 2020). These earthquakes typically induce crustal deformation affecting the ground surface and sea floor, and result in catastrophic consequences both along the coast and inland (e.g. 1985 Michoacán earthquake).

2.2. Geology, geomorphology and climate

The lithology of the coastal bedrock in the epicentral area is dominated by a thick sequence of Cretaceous pelitic and reef carbonates, interbedded with horizons of andesitic, dacitic, and volcaniclastic rocks

(González-Partida and Torres-Rodríguez, 1988; Barrios et al., 2000; CONAGUA, 2020). Intrusive rocks also outcrop, mainly in the coastal region near Maruata (Fig. 1), where the predominant lithologies are calc-alkaline granitoids and diorite. These rocks intrude both metamorphic rocks and the predominant Cretaceous volcano-sedimentary sequences in the SW of the state of Michoacán. Radiometric ages obtained for these rocks range from the Late Jurassic to the Miocene (Fuentes-Farias et al., 2010; INEGI (Instituto Nacional de Estadística y Geografía), 2010). The epicentral area of the 2022 earthquake is located within the physiographic province of the Sierra Madre del Sur (INEGI Instituto Nacional de Estadística y Geografía, 2023a). Geomorphologically, two main units are distinguished: a) the coastal belt, corresponding to a narrow coastal plain with a flat shape and a gentle slope towards the sea; characterized by wider plains with coastal lagoons; b) the mountain area or *sierra*, characterized by steep slopes, an incised relief and a mean elevation of 2000 m asl (above sea level).

Between El Faro and La Majahuita the mountains and hills of the Sierra Madre del Sur dive into the sea while drawing a winding coastline, practically without a coastal plain (Fig. 1, 2). The average annual temperature in the coastal area is 26 °C, with the warmest months occurring from May to October (INEGI Instituto Nacional de Estadística y Geografía, 2023a). The average annual precipitation is 1032 mm, with the rainy season extending from June to September and an average of 164 mm/month. In the *Sierra* area, the average annual temperature is 23 °C. The average annual precipitation in this area is 1397 mm, with the rainy season occurring from June to October (average 256 mm/month) and the dry season from November to May (average 31.75 mm/month).

2.3. Historical seismicity

The instrumental seismic record in Mexico over the last 120 years has documented the occurrence of 23 earthquakes of $M_w \geq 7.5$ within the northwestern part of the Mexican subduction zone (SSN, 2023; Fig. 2). Notable among them are the Jalisco earthquakes on June 3rd, 1932 (Ms 8.2) and June 18th, 1932 (Ms 7.8); the Michoacán earthquakes on April 15th, 1941 (Ms 7.7), January 30th, 1973 (Mw 7.6), and September 19th, 1985 (Mw 8.0); the Colima-Jalisco earthquake on October 9th, 1995 (Mw 8.0); the Colima earthquake on January 22nd, 2003; and finally the Michoacán earthquake on September 19th, 2022, which is the subject of this study (Mw 7.6; Ruff and Miller, 1994; Pérez-Campos et al., 2018; Singh et al., 2023a, 2023b; Fig. 1, 2).

Strong pre-instrumental earthquakes are documented as well (Suárez and Albini, 2009; Suter, 2019).

2.3.1. The January 30th, 1973 and September 19th, 2022 events: "Twin earthquakes"

On January 30th, 1973, at 21:01:12.52 GMT, a megathrust earthquake of M_w 7.6 occurred at 16 km depth along the interface of the Cocos and North American plates. The epicenter was located at 18.49° N latitude and 102.89° W longitude, approximately 160 km southeast of Manzanillo, Colima (Fig. 2; Figueroa, 1974; Santoyo et al., 2006; Singh et al., 2023a).

Figueroa (1974) and Reyes et al. (1979) documented the earthquake effects in Michoacán and Colima states. Affected area spanned 450,000 km^2, with intensities ranging from III to VIII on the MM scale (Figueroa, 1974). Numerous cities and towns experienced severe damage, with the city of Tecomán, located 100 km northwest of the epicenter, being particularly hard-hit (Reyes et al., 1979). 48 fatalities and 505 injuries were reported (Figueroa, 1974).

The documented earthquake environmental effects included tree shaking, hydrogeological anomalies like fluctuations in spring water levels, alterations in piped water flow, slight subsidence in specific regions, landslides, potential dust clouds (referred to as smoke columns on the Colima volcano), underground noise, liquefaction leading to terrain cracking and fractures, and anomalous waves (Figueroa, 1974).

During the two fieldwork campaigns in the epicentral zone of the 2022 earthquake, residents not only mentioned the seismic event of 1973 but also emphasized the 1941 earthquake. The impacts of the 1941 earthquake were comparable and, in some cases, even more intense, particularly in phenomena like ground cracking, fractures, liquefaction, and landslides.

The epicenters of the 2022 mainshock and aftershocks overlap the area affected by the 1973 sequence (Liu et al., 2023; Singh et al., 2023a). According to Singh et al. (2023a), their similarity and location makes them twin Mw 7.7 megathrust earthquakes, with a recurrence interval of approximately 50 years. This recurrence interval is consistent with the relatively short average recurrence interval between 30 and 50 years observed for large events rupturing other segments of the Mexican subduction zone (Liu et al., 2023; Singh et al., 2023a, 2023b).

3. The September 19th, 2022 earthquake

On September 19th, 2022, at 13:05:09 local time, a M_w 7.7 earthquake (SSN, 2022), ruptured the NW boundary of the interface between the Cocos and North American plates (Singh et al., 2023a; Fig. 1 and 2). The epicenter was near Coalcomán, Michoacán, at 18.24° N latitude and − 103.29° W longitude (Fig. 1). This earthquake is an interplate megathrust event, with a relatively shallow hypocenter (H = 15 km) and reverse fault focal mechanism (Fig. 2).

An integrated analysis of geodetic, tsunami, and teleseismic observations has identified a slip patch extending roughly 80 km along the strike and situated between 10 and 30 km depth, highlighting a maximum slip of about 2.9 m (Liu et al., 2023). The earthquake showed a unilateral propagation towards the NW (Singh et al., 2023a; Fig. 2). The epicenter and subsequent aftershocks are contained within an area previously affected by aftershocks stemming from a similar magnitude earthquake in 1973 (Fig. 1).

The impact of the 2022 Michoacán earthquake as felt by humans and observed in built environment, shows a bias driven by population density. The 2022 Michoacán earthquake produced five casualties (three in the state of Colima and two in Mexico City) and widespread damage to infrastructure, essentially along the Pacific coast in the epicentral area (Miranda et al., 2022). Fig. 3a presents the location of eyewitness accounts collected by the "*¿Sintió un sismo?*" program (Montalvo-Arrieta et al., 2017). Individuals who have experienced an earthquake can fill an online form available on the website of the Universidad Autónoma de Nuevo León and the SSN. The data are compiled by the system and published in the form of maps minutes after significant earthquakes, continuously updating as additional data is received. To our knowledge, as of yet the "*¿Sintió un sismo?*" data in Fig. 3a are the only original macroseismic information available for the September 19th, 2022, earthquake. Fig. 3b shows the population density and the epicenter location. The population density is retrieved from the Landscan database, which represents an ambient population (average over 24 h) distribution on a raster of about 1 km^2 resolution. The uneven distribution of the population affects the availability of crowdsourced data: by comparing the two panels of Fig. 3, it is evident that a higher number of responses to the "*¿Sintió un sismo?*" program is obtained from more populated regions. In the following, we describe in detail the macroseismic effects generated by this earthquake on the natural environment.

4. Methods

4.1. Documentation of earthquake environmental effects (EEEs)

The EEE documentation is based on three complementary approaches, that are 1) field reconnaissance, 2) data collection from online resources, and 3) landslide mapping from satellite images. For the data collection, we followed the same methodology as in Velázquez-Bucio et al., 2023a.

These three methodologies yielded distinct datasets with varying

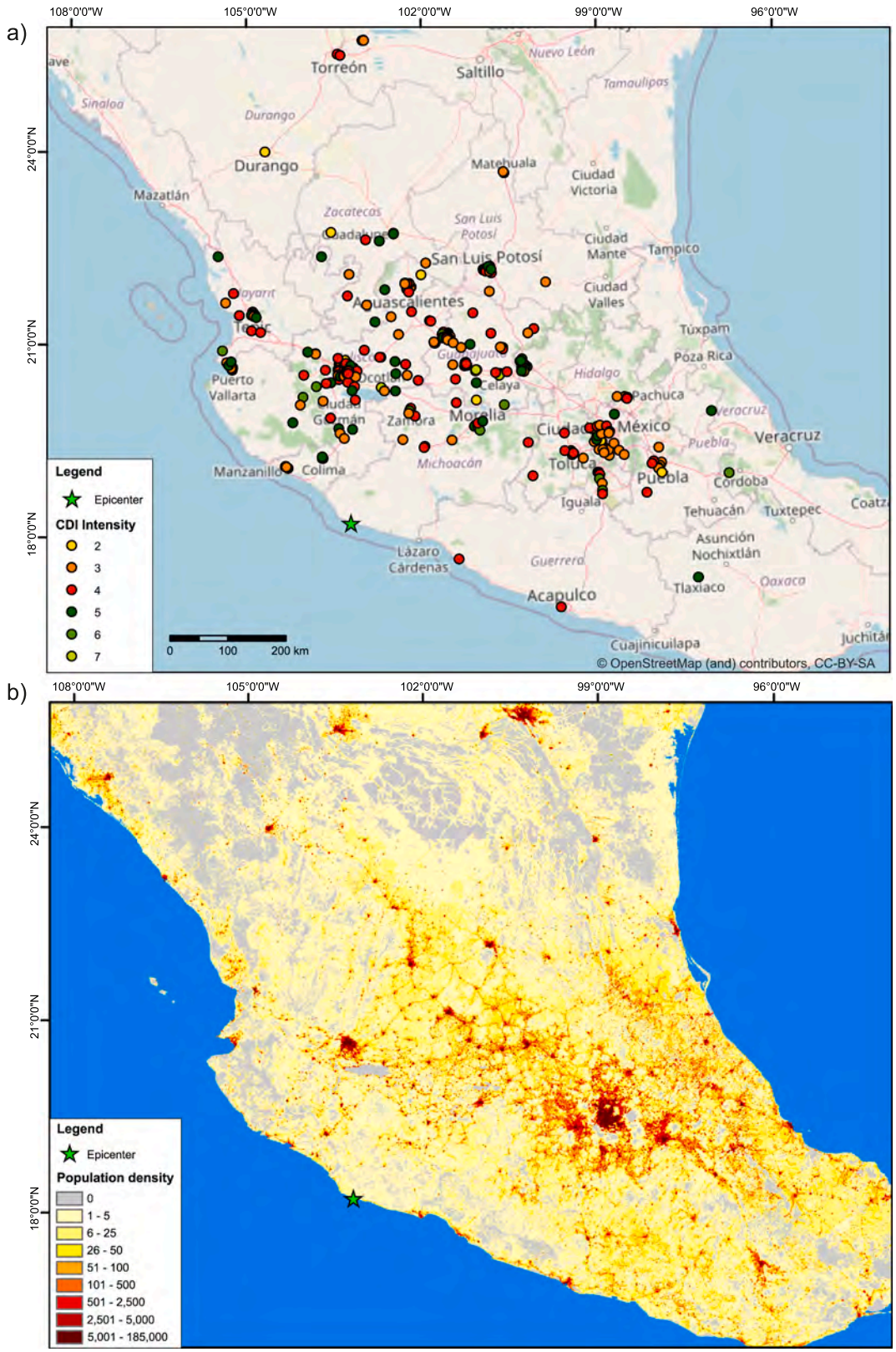

Fig. 3. a) Macroseismic effects recorded using the "*Sintió un sismo?*" platform (Montalvo-Arrieta et al., 2017), expressed in terms of CDI (Community Decimal Intensity), Basemap © OpenStreetMap Distributed under the Open Data Commons Open Database License (ODbL) v1.0; and b) Map of population density in Central Mexico, note the low density in the epicentral area of the 2022 Michoacan earthquake compared to nearby regions (Landscan dataset; Rose et al., 2023). (For interpretation of the references to color in this figure legend, the reader is referred to the web version of this article.)

degrees of spatial coverage and overall data quality in terms of EEE documentation. By integrating data from these diverse approaches, we aimed to provide a more comprehensive depiction of the earthquake effects.

4.1.1. Field surveys

We conducted two field surveys, one during the 4 days immediately after the earthquake and a second six months later, from March 12th to 15th, 2023 (Fig. 1). We collected precise site descriptions and measurements and detailed photographic documentation. During these surveys, we observed the primary, tectonic effects of the earthquake to the NW of the epicenter. At each site, eyewitness interviews confirmed the coseismic nature of the observed coastal uplift. We measured vertical displacement using intertidal organisms as biomarkers of this elevation change. In order to use displacement of the intertidal biome as precise elevation datum, we first carried out a detailed analysis of the habitat, morphology, and distribution of these organisms. To determine the vertical displacement of the fringe of exposed sessile organisms, we took measurements from the top of the filamentous portion of the algal population, which is currently exposed to moisture, to the point at the top where the organisms showed signs of desiccation, discoloration, or alterations in their morphology. In order to calculate the vertical displacement with the highest possible accuracy, for each measurement taken, the measurement time and tidal variations were adjusted relative to a reference level, using the tide gauges provided by CICESE (CICESE, 2022, https://predmar.cicese.mx/calendarios/). This way, we excluded the influence of tides on the vertical displacement value caused by the earthquake.Coralline algae proved to be particularly effective indicators, as they change color after their death. Following the earthquake, populations of these algae were exposed to dehydration conditions and subsequently death due to desiccation. In addition to the organisms indicating uplift, we employed the exposure of “fresh rock” and tidal notches to quantify the primary effect of tectonic uplift on the environment. In areas where the exposure of organisms was not observed, the accounts of local residents as well as the formation of small terraces were used for quantification of uplift. It should be noted that our two measurement surveys occurred several days and several weeks after the mainshock, respectively; therefore, they might include minor post-seismic deformation. For the documentation of secondary effects, we collected the quantitative measures more useful to obtain an ESI-07 estimate (see Sect 4.2).

The field surveys have limitations due to time and spatial constraints, often restricted to specific areas; it should be noted that most of the epicentral area is not directly accessible due to difficult logistics and security issues.

The geological and geomorphological characteristics of the affected area, combined with the peculiarities of the seismic source and the event itself, can exert a significant influence on the manifestation of the EEEs diversity. Indeed, the environmental effects of an earthquake tend to dissipate rapidly within days or weeks. The influence of climatic conditions of the region and human activity accelerates this process, highlighting the importance of collecting information immediately after the event. In fact, significant rainfall occurred in the days following the earthquake. It should be taken into account that rainfall modified and eroded coseismic environmental effects such as ground cracks, landslides and sand volcanoes. However, the areal distribution, number and dimensions of the identified ground effects is very large, and we are confident that the final ESI-07 assessment is reliable enough.

4.1.2. Data compilation from online sources

We collected information from publications, local media sources such as online newspapers, government reference sites, and social media platforms like Twitter©, Facebook©, Instagram©, TikTok©, and YouTube©. The search was realized both in Spanish and English; we used keywords like “earthquake, seismic event, vibration, landslide, earthquake effect” to extract relevant data. In the case of social media content, we also used filters based on the date of the post.

We repeatedly checked for information and updates from official institutions, including the *Universidad Nacional Autónoma de México* (UNAM), *Servicio Sismológico Nacional* (SSN). Moreover, we looked for scientific publications or technical reports on instrumental seismicity, geodesy and source modeling (e.g., Singh et al., 2023a; Liu et al., 2023).

This second approach compensated for some of the limitations associated with field surveys but still faced challenges related to time and spatial constraints, as accurate data acquisition is usually limited to a specific area. All the collected data were subsequently analyzed to extract an optimal geolocation based on the spatial quality of the source, and assessed with objectiveness.

4.1.3. Landslides mapped from satellite images

We mapped landslides in the epicentral area from visual inspection of satellite images provided by Planet under an educational license. The investigated area has a dimension of ca. 10,000 km^2 (dashed green line in Fig. 2). Cloud cover was intermittently present over the area, so we searched for cloud-free imagery exploiting both daily Planet images and monthly basemaps. As pre-earthquake images, we used the August 2022 basemap and tiles acquired on September 7th and 8th, 2022; for post-earthquake images, we used the October 2022 basemap and tiles acquired from September 25th, 2022 to October 31st, 2022. The orthorectified images have a resolution of 3 m.

We digitized landslides in QGIS on a 1:5000 scale. Mapped polygons encompass the source and deposit area and were identified based on the change in color and texture on the pre- and post-event imagery. The identification of landslides was straightforward in forested areas, since slope movements stripped off the vegetation, whereas it was more difficult in cultivated areas where changes may be due to farming activities: in this case, we checked multiple post-event images to identify only the changes due to slope movements. In the case of pre-existing landslides (i.e., already present in the pre-earthquake imagery), we mapped them only if they were clearly retriggered.

4.2. ESI-07 evaluation

The 12 degrees of the ESI-07 scale relate to earthquake strength and provides a measure of its intensity (Michetti et al., 2007; Serva et al., 2016), assigned through a quantitative analysis of EEEs (Papathanassiou et al., 2017a, 2017b; Naik et al., 2023b). We carried out the evaluation of the EEEs carefully following the guidelines of the ESI-07 scale guide (Michetti et al., 2007). The ESI-07 scale is organized according to three hierarchical levels: sites, localities and earthquake (Michetti et al., 2007; Serva et al., 2016). A “Site” is a single place where a specific EEE is observed; the evaluation of the ESI-07 intensity at each site is based on specific numerical metrics (e.g., amount of uplift/subsidence; length and width of ground cracks; dimension of liquefaction sand boils; volume of slope movements). A “Locality” is an area of limited extent (in the order of hundreds of meters to few kilometers) which might include different “Sites”; for instance, a sector of alluvial plain where several sites with coseismic liquefaction occurs very close to each other. A “Locality” has a level of generalization to which an intensity value can be assigned. The “Earthquake” level refers to the EEEs generated during a specific seismic event observed as a whole. For instance, at the “Earthquake” level we assess the isoseismals and the epicentral intensity Io (Michetti et al., 2007).

For sites where coastal uplift was observed, we determined the ESI-07 intensity value by evaluating the vertical displacement of organism communities, including coralline algae and barnacles. This assessment takes into account factors such as habitat type, species distribution, and morphologic analysis, while also adjusting for tidal variations based on the sampling time.

Concerning the landslides mapped remotely, we used a scaling relationship to convert area to volume. Indeed, in the ESI-07 framework (Michetti et al., 2007), an intensity value is assigned to slope movements

based on their volume. Additionally, landslide dimensions saturate at ESI-07 X, which means that slope movements with volumes higher than 10^6 m^3 correspond to intensity ≥ X thus, it is not possible to assign local ESI-07 values of XI and XII to landslides. Several area-volume relations are available in the literature (e.g., Guzzetti et al., 2009; Xu et al., 2016; Fan et al., 2019) which mostly assume the form of Eq. 1:

$$V = \alpha \times A_i^{\gamma} \quad (1)$$

where V is the volume (m^3), A_i is the area of the i-th landslide (m^2), α and γ are fitting coefficients. We used the α and γ derived by Larsen et al. (2010) on a dataset of global earthquake-triggered landslides, i.e., α = 0.146 and γ = 1.332. As threshold values for each intensity degree, we applied the same values of Ferrario (2022), which also showed that the selection of a specific area-volume relation does not heavily affect the ESI-07 assignment, since ESI-07 values are based on broad categories spanning order of magnitude in terms of mobilized volumes.

Based on the threshold values provided in the ESI-07 scale (Michetti et al., 2007), we assigned an intensity value to each site.

We described each EEE identified during the field surveys, and then data were organized according to the guidelines outlined by Michetti et al. (2007). This description takes into consideration various factors, including the lithologic, stratigraphic, hydrogeologic, and local geomorphologic context, as well as the dimensions or volume of the observed effects. Subsequently, each EEE is categorized as either a primary or secondary effect. Primary effects are directly related to the seismic source and its surface manifestations, while secondary effects are triggered by ground shaking, and influenced by the unique characteristics and conditions of the local environment (Michetti et al., 2007; Guerrieri et al., 2015; Serva et al., 2016).

Finally, we used the individual EEE sites to draw isoseismal contours, representing areas which experienced the same level of damage, i.e., share a common intensity value. If multiple effects were observed in a close area ("Locality" level; hundreds of m – few km), we retain the highest intensity value, following the ESI-07 guidelines and criterion carefully described in the original papers introducing the ESI-07 Scale (Michetti et al., 2004, 2007; Serva et al., 2016). The drawing of the isoseismals lines, in this way, repeats the classical methodology through a professional judgment of experience, used as in the case of all the others macroseismic scales that take into account in the areal distribution of intensity above all the highest values, which are those that can most play a predominant role in the definition of the hazard of the area investigated. It is possible that within the higher grade of isoseismals lines there are locations with significantly lower intensities, but this depends on the more or less complex local conditions for which detailed

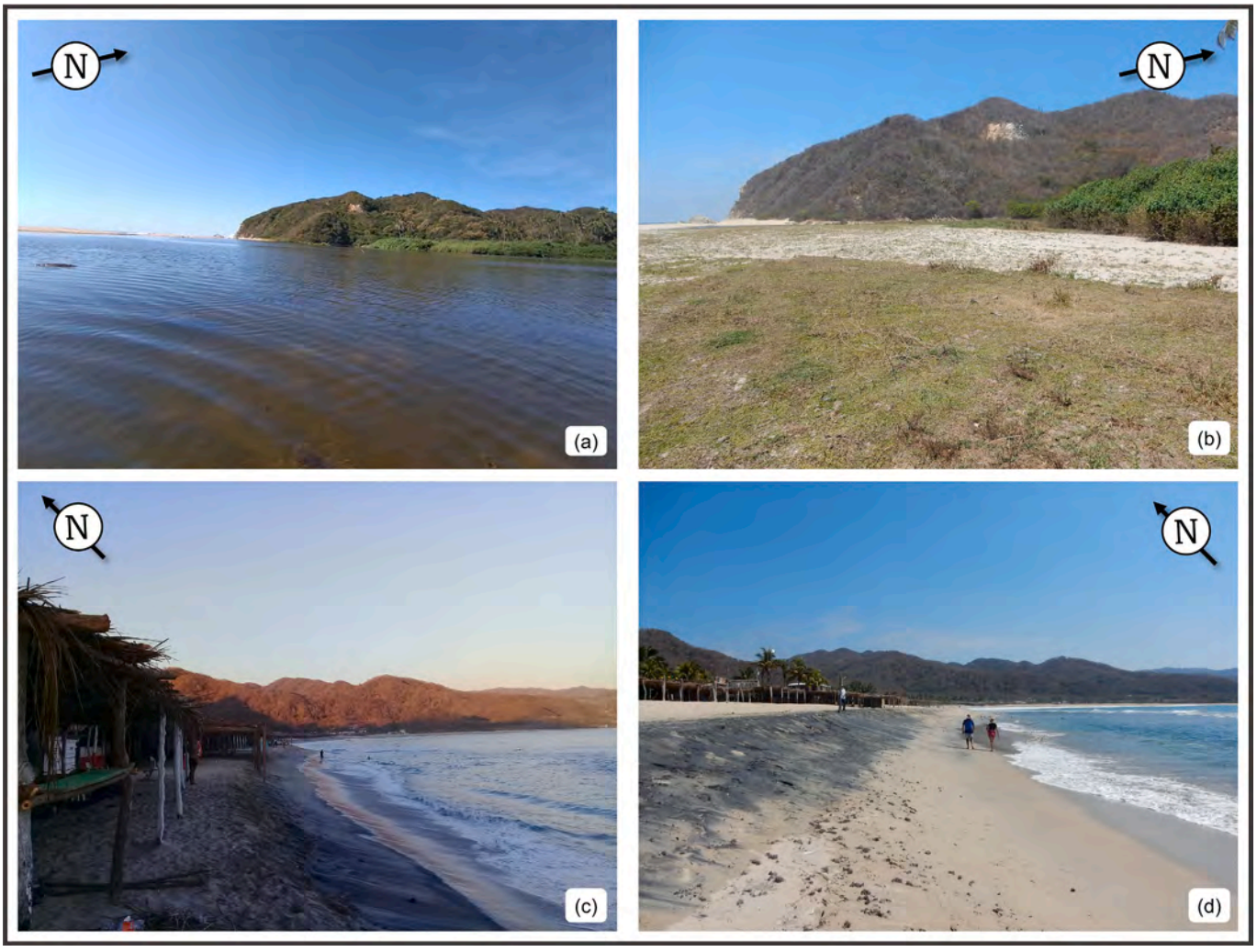

Fig. 4. Primary effects, coastal uplift: a, b) lagoon on Motín del Oro locality, before (a; from © Facebook, Playa_Motín_Del_Oro_Michoacán, 2020) and after (b; our picture during fieldwork on March 2022) the mainshock; note the difference in the landscape, water level in the lagoon before and after the earthquake; permanent drying of the lagoon corresponding to 83 cm of coseismic coastal uplift at Motín del Oro locality at 21.5 km from the epicenter; c,d) Maruata beach, the difference in water level and beach width between the palm-thatched shelters (palapas) and the sea is evident, before (c; from © Facebook, Coastal_uplift_Maruata, 2019) and after (d; our picture during fieldwork on March 2022) the earthquake, in the locality of Maruata; I = X ESI-07. See Fig. 5 for locations.

analyses should be carried out later to explain the lower estimate.

5. Results

We documented 8070 EEEs resulting from the September 19th, 2022 earthquake: 120 were directly observed in the field; 12 sourced from scientific publications; 19 obtained from news reports; 25 gathered from social networks; and 7894, all landslides, using satellite images. The ESI-07 intensity values of the EEEs sites vary from IV to X. Coseismic effects encompass both primary effects (permanent ground deformation, associated with coastal uplift) and secondary effects (liquefaction, lateral spreading, cracking, slope movements, hydrogeologic anomalies, tsunami).

5.1. Primary effects: Coastal uplift

We observed vertical displacement of shoreline features at several locations (Figs. 4 and 5) along the coast extending at least 60 km NW of the epicenter. The length of 60 km is a minimum estimate, since we were not able to extend our observations SE of the epicenter. This limitation is due to both logistical and security reasons, which prevented us from visiting the entire coastal strip in the epicentral area.

We measured permanent ground deformation of the shoreline a few days after the earthquake in a first campaign and six months later in a second campaign, using various indicators, mostly on rocky coasts. Similar to what is described in the literature for large subduction events on the SE Pacific (e.g., Ortlieb et al., 1996; Castilla et al., 2010; Chunga-Llauce and Pacheco, 2021), these indicators include a) impacts on rocky intertidal habitats, changes in the color and morphology of intertidal organisms, which became apparent as they were suddenly exposed to

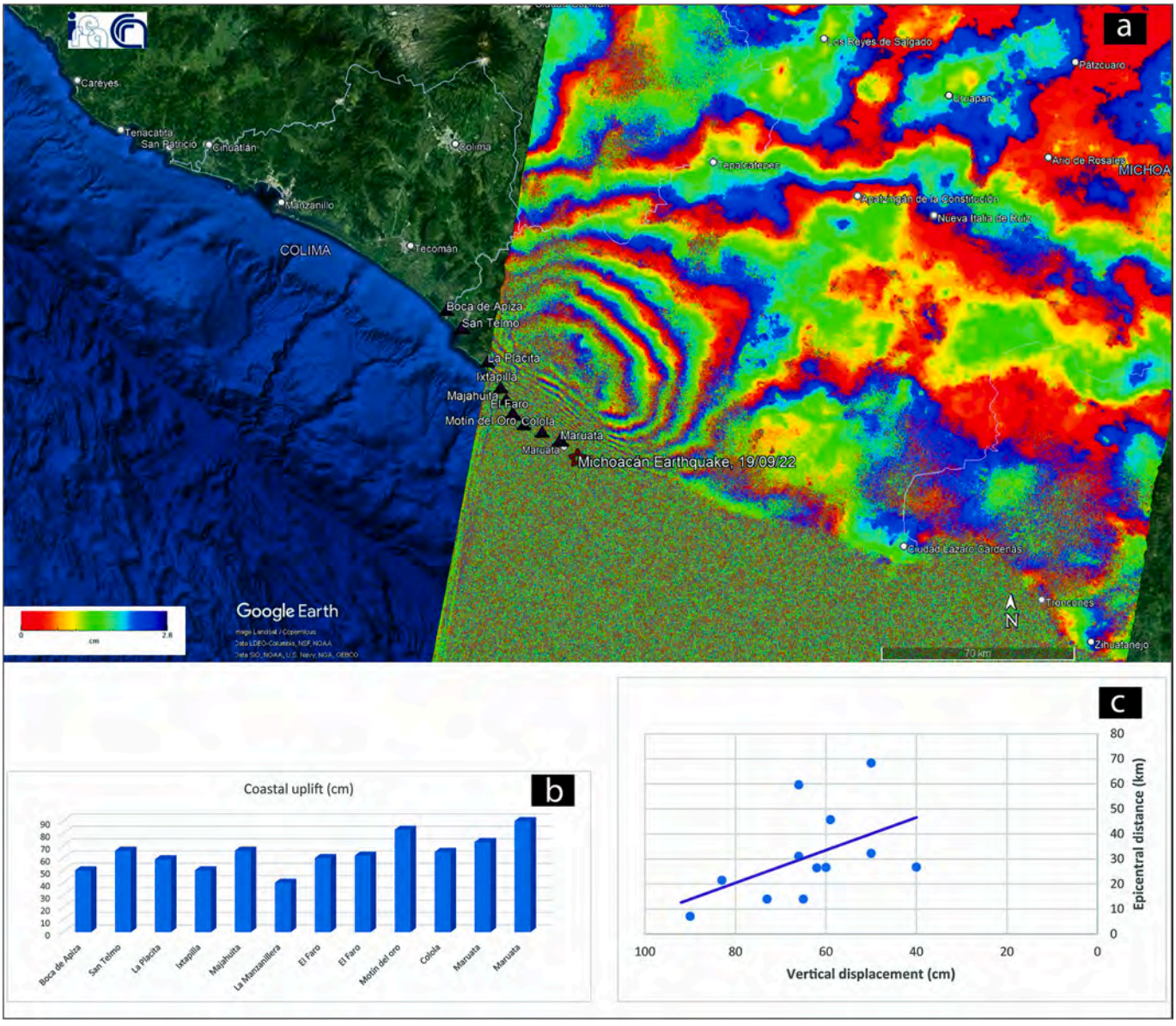

Fig. 5. Distribution of the primary effect in relation to the epicenter. a) Differential interferogram generated from satellite imagery in descending orbit 12, Satellite Platform S1, covering the period from September 18th, 2022, to September 30th, 2022 (Processing Service EPOSAR and data provided by CNR-IREA, courtesy of Fernando Monterroso). InSAR data highlight the consistency between coastal uplift measurements in the field and the area with the greatest deformation extending from the epicenter towards the northwest. Small triangles indicate locations with evidence of coastal uplift as in Table 1. Basemap © Google Earth and contributors. b) Graph illustrating degree of coastal uplift measured at each locality. c) Vertical coastal displacement versus the epicentral distance.

sunlight and perished from desiccation; b) impacts on rocky subtidal habitats, with subtidal rocks permanently exposed after the earthquake; c) impacts on soft-bottom intertidal habitats, with small terraces formed, and the beach area expanded.

The distribution of species in intertidal areas is intricately influenced by a combination of both biotic and abiotic factors closely associated with tidal cycles (Bodin and Klinger, 1986). Any significant and abrupt physical or chemical alteration can result in a profound transformation of the species associations and of the entire ecosystem. In the upper intertidal zone, the extent of air exposure emerges as a pivotal factor in defining the upper range limit of certain sessile species (Bodin and Klinger, 1986). For instance, a substantial increase in elevation, caused by phenomena such as an earthquake, can lead to the mortality of certain sessile species whose upper boundaries are determined by the duration of exposure during low tide (Bodin and Klinger, 1986; Ortlieb et al., 1996; Castilla et al., 2010).

A fringe of dead and discolored coralline algae was observed and measured at eight localities from Maruata to San Telmo. The coastal uplift along this stretch increases tendentially from 50 to 90 cm towards the SE, that is getting closer to the epicenter (Fig. 5). Some of these organisms were identified at the genus level, in addition to species of barnacle, *Balanus balanoides* (Fig. 6 and Table 1).

In areas devoid of rock exposure or of a sessile organism fringe, such as El Faro and Ixtapilla, the accounts of the residents and the observation of an increase in the extent of the shore zone and small raised beach terraces formation support coastal uplift as the determining factor. Collected data and measurements are consistent with the results obtained from biomarkers and comparable measurements taken in the localities where we observed exposed and dead organisms (Table 1, Fig. 5, 6).

Coastal uplift is not strictly continuous, particularly towards the NW end of the uplifted section. However, the relationship between vertical

Fig. 6. Pictures showing fringe of dead and discolored barnacles and coralline algae raised by the coastal uplift; a) at El Faro locality; b) Colola locality; c) San Telmo locality, coralline algae biomarker; d) Majahuita locality; barnacle *Balanus balanoides* (Linnaeus, 1758) species, coastal uplift biomarker. See Fig. 5 for locations.

Table 1
Measured coastal uplift due to regional tectonic displacement during the earthquake of September 19th, 2022; ID corresponds to the identification number in the database of the registered EEEs (Velázquez-Bucio et al., 2023b); measurements were carried out on the days of 24-25th September 2022, and 14-15th March 2023.

ID	Site	Bio-indicator	Displacement (cm)	Epicentral distance (km)	ESI-07	Measurement date
147	Boca de Apiza		50	68	X	14/03/2023
174	San Telmo	Coralline algae	66	60	X	15/03/2023
154	La Placita		59	46	X	14/03/2023
156	Ixtapilla		50	32	X	14/03/2023
158	Majahuita	*Balanus balanoides*	66	31	X	14/03/2023
159	La Manzanillera		40	27	X	15/03/2023
51	El Faro		60	27	X	24/09/2022; 15/03/2023
119	El Faro	Coralline algae	62	26	X	24/09/2022; 15/03/2023
171	Motín del oro	Filamentous algae	83	22	X	15/03/2023
164	Colola	Coralline algae	65	14	X	15/03/2023
57	Maruata		73	14	X	25/09/2022; 15/03/2023
113	Maruata	*Ulva lactuca*	90	7	X	25/09/2022; 15/03/2023

displacement and epicentral distance reveals a gradual deformation trend, decreasing from the area closest to the epicenter towards the NW. Within a tendency for the vertical displacement to increase towards the epicenter, the most distant locality, Boca de Apiza, recorded a displacement of 50 cm, increasing to 66 cm in the localities of San Telmo, but decreasing in La Placita, which recorded 59 cm (Fig. 5 and Table 1). Along the coastline, the width of the biomarker fringe irregularly decreases NW-ward as we move away from the epicentral zone, almost disappearing beyond 60 km.

Possible factors contributing to the variability and discontinuous displacement in the terrain along the coast of Michoacán, where we observed coastal uplift, include variable seismic slip, different rheology in different zones, and varying subduction thrust fault dip angles (Bodin and Klinger, 1986). However, the region with coastal uplift identified during the two fieldwork campaigns aligns seamlessly with the displacement models of the area affected by the September 19th, 2022, Michoacán earthquake, analyzed and processed by INEGI (2023b) and CNR-IREA and INGV (Atzori et al., 2023; Fig. 5).

5.2. Secondary effects

5.2.1. Ground cracking

Ground cracks appeared in various natural environments such as terrains (Fig. 7a), beaches, river and lake shores; and along dirt roads and asphalt surfaces. At 36 sites, ground cracks intercepted and damaged buildings and infrastructures, including house foundations, restaurants, roads and highways. This effect was primarily observed in the zone that experienced coastal uplift. Beyond the deformation area, cracks were recorded at a maximum distance of 165 km from the epicenter, in Manzanillo, Colima. The dimensions of these cracks varied, ranging from a few centimeters to several tens of centimeters, especially in areas with loose soils, such as riverbanks, canals, and roads. The width

Fig. 7. Pictures showing examples of secondary effects: a) ground cracks of 30–100 cm width and about 200 m length observed in Maruata, Michoacán; b) localized lateral spreading of more than 30 cm and settlement with fissuring parallel to waterfront areas registered in Coahuayana Viejo, Coahuayana, Michoacán (from © Facebook, Luciérnaga Noticias, 2022); c) rockfall with blocks of diameter reaching up to 3 m, with material falling from an unstable slope of a cliff, observed in Las Brisas, Michoacán; d) liquefaction and wide cracks in pavement observed in the area between Ticuiz II bridge, Coahuayana and Ticuiz road, Coahuayana, Michoacán; e) close up of a huge block of a rockfall of 10^5–10^6 m^3 volume, observed between Tepalcatepec and Aquila Road, Huitzontla, Chinicuila, Michoacán (Courtesy of Ing. Antonio de J. Mendoza C.; SSN); f) hydrogeological anomaly recorded in Aquila, Michoacán; turbidity of this spring water and its subsequent drying.

of these cracks was less than 1 cm on some roads, an average of around 10 cm on highways and bridges, and reached up to 50 cm at Mezcala Beach, with a maximum depth of 53 cm in compact material under the sand, and 55 cm at San Vicente with 100 m length, on a natural fill road. In structures like road bridges, some of the cracks displayed a few centimeters of vertical displacement due to destabilization and structural impact. In natural soils, cracks exhibited vertical displacement up to 19 cm, but only in fill soils. The intensity range for this effect on the ESI-07 I═VI – X.

5.2.2. Landslides

We mapped a total of 7894 earthquake-triggered landslides, resulting in an average density of ca. 0.8 landslides/km^2; the total landslide area (i.e., sum of areas of individual polygons) reaches 7.43 km^2, representing 0.08 % of the investigated area, while the average dimension of individual landslides is 940 m^2.

It should be noted that our inventory is a compilation of landslides visible in the post-event imagery, which was acquired no more than one month after the earthquake. This time frame includes the mainshock, aftershocks and other processes such as rainfall; however, we are confident that a major role is due to the seismic sequence, since landslides were not present before the mainshock. According to Jibson and Tanyaş (2020), earthquakes with magnitudes greater than Mw 6.5 can cause large landslides due to the longer duration and higher frequency of the seismic movement. The study by these authors indicates that the average duration of earthquakes with magnitudes between 6.5 and 8 ranges between 25 and 100 s. Liu et al. (2023) observed a duration of around 80 s for the 2022 Michoacán earthquake, supporting the correlation between earthquake intensity and landslide size.

Fig. 8 presents a comparison of images acquired before (September 2nd, 2022) and after (October 31th, 2022) the mainshock. Landslides can be clearly identified in the satellite images due to the change in color and locally show long runouts (e.g., Fig. 8b). The landslide dimension is variable in the investigated region, with areas ranging between about 20 and 4200 m^2. Such values correspond to local ESI-07 intensities of VI to IX, obtained using the area-volume relation proposed by Larsen et al. (2010).

We investigated the spatial distribution of landslides by computing the density and areal percentage on a grid of 1 km^2 cells. Landslide number density (LND) reaches values as high as 60 landslides/km^2; highest values are found in a region located ca. 45 km NW of the epicenter (Fig. 9a). Landslide area percentage (LAP) represents the amount of territory covered by the coseismic landslides, computed on a regular grid; highest values reach 6.9 %, in the same region where maximum LND values are found (Fig. 9b). The highest landslide concentration, either in terms of LND and LAP, is located NW of the epicenter, in a NW-SE oriented stripe, which may be related to seismological parameters (e.g., rupture directivity), the distribution of predisposing factors (e.g., slope, lithology) or a combination of both.

Fig. 9c shows the area-frequency distribution of the inventory: the probability density is computed following Malamud et al. (2004) as:

$$p = \frac{1}{N}\frac{\delta N_L}{\delta A_L} \tag{2}$$

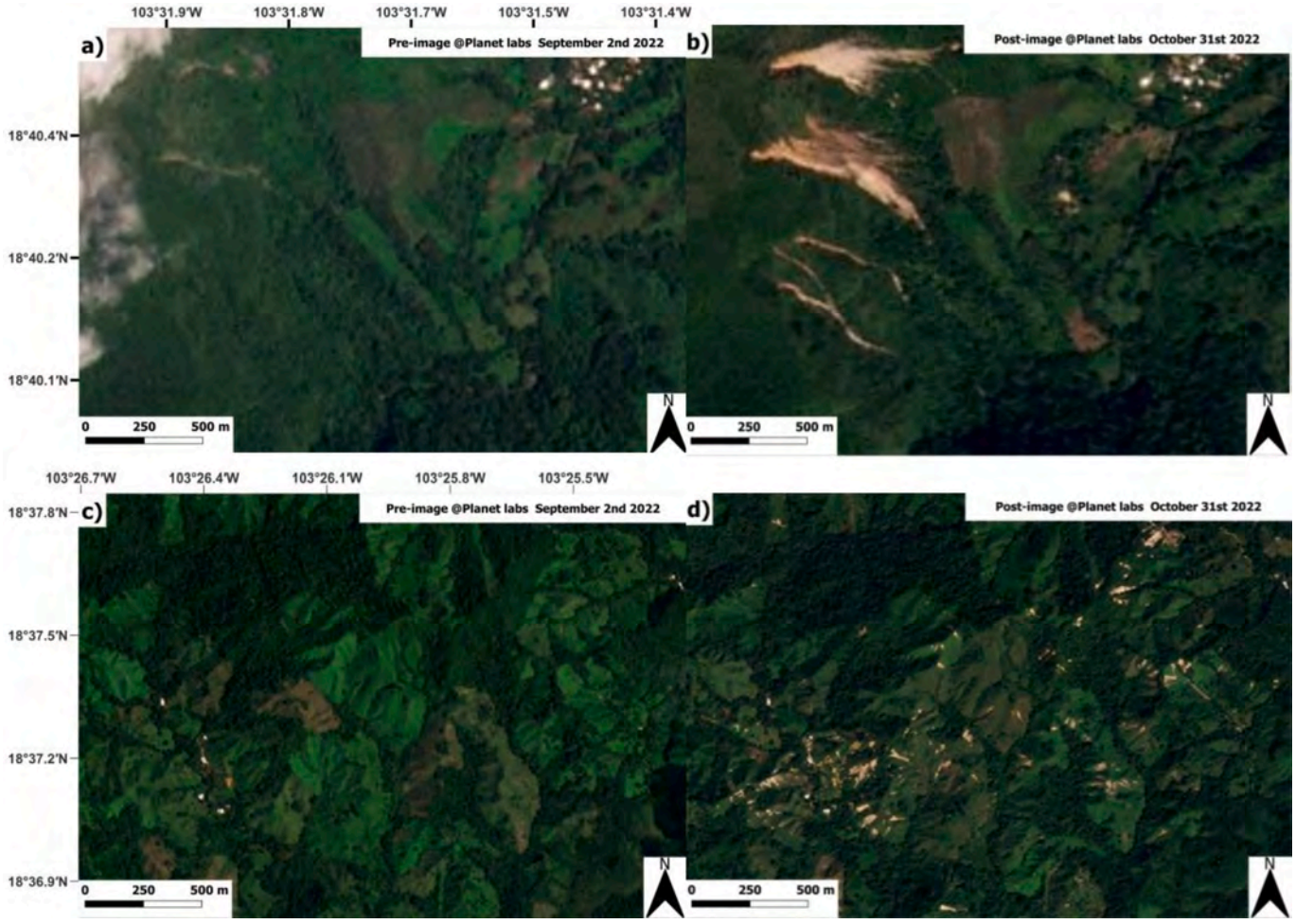

Fig. 8. Satellite images used for landslide mapping from Planet labs images; panels a) and c) show the pre images while b) and d) show the post images from the same area; upper panels show a set of large slope failures with long runouts, while lower panels show densely distributed smaller landslides with a more regular shape.

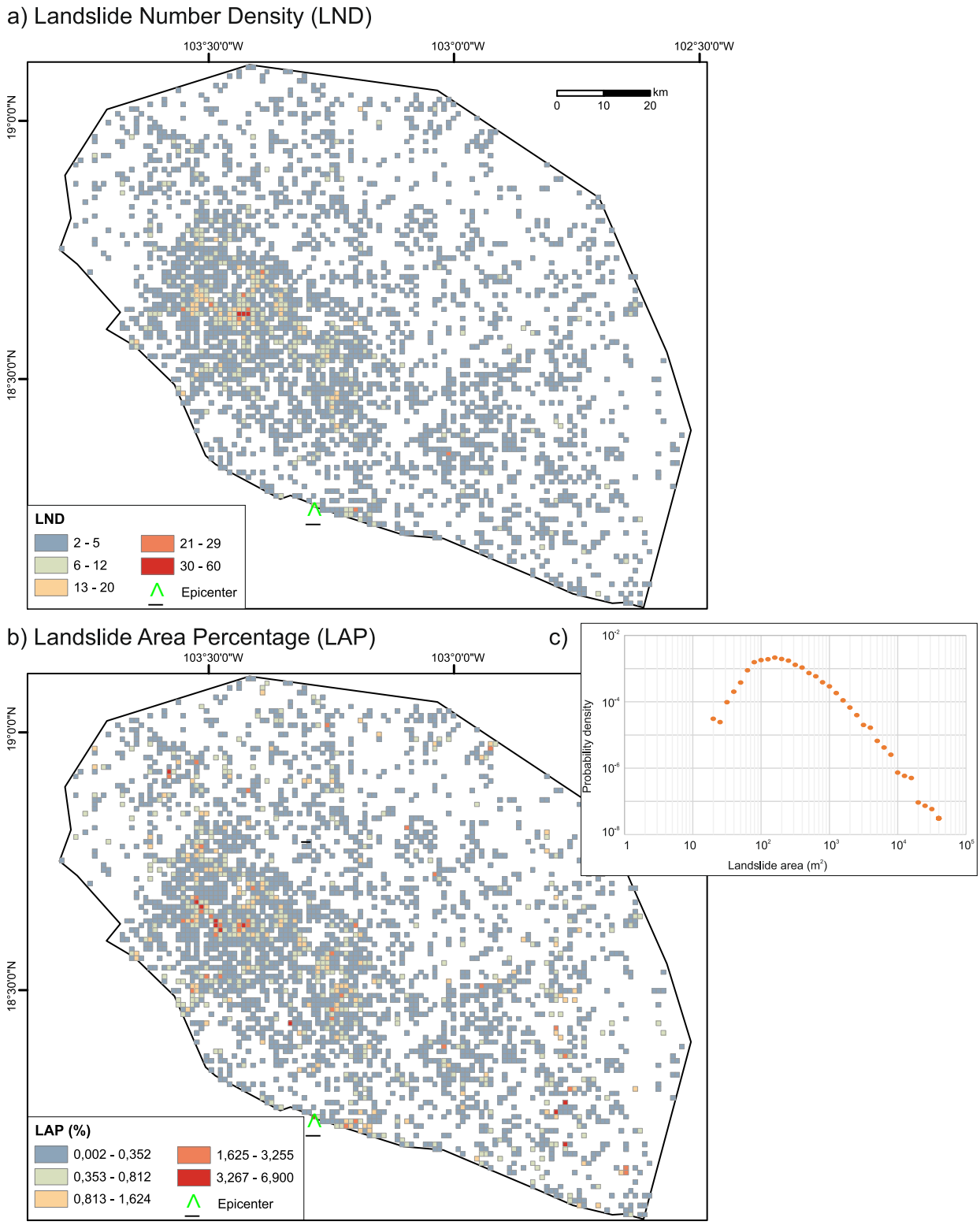

Fig. 9. Landslides mapped using satellite imagery, the outline of the investigated area is shown in Fig. 2; a) Landslide density number (LND), computed on a grid of 1-km^2 cells; b) Landslide area percentage (LAP), computed on the same grid as LND; c) non-cumulative landslide-area distribution of the inventory mapped in this study.

where N is the total number of landslides, N_L is the number of landslides with area between A_L and $A_L + \delta A_L$; bin width is equal in logarithmic coordinates.

Our inventory shows a rollover point at ca. 150 m^2; this value, which is seen as a proxy for the minimum dimension for which the inventory is complete, is quite small with respect to global compilations of earthquake-triggered landslides (e.g., Tanyas and Lombardo, 2020). Moderate to large landslides (i.e., the right tail of the curve) follows a negative power law scaling, with an exponent of −2.15, in broad agreement with other case studies (e.g., Van der Eeckhaut et al., 2007;

Tanyas et al., 2018).

5.2.3. Liquefaction

Saturated soils are especially prone to liquefaction during an earthquake. The area near the epicenter of the Michoacán earthquake is particularly vulnerable to this effect, due to both its lithological, geomorphological and climatic conditions. In addition, the rains that occurred before the event favored liquefaction but the ones occurred after erased surface features and evidence in areas such as beaches and river banks. However, evidence of liquefaction remained in locations where it affected human infrastructures, such as plaza floors, housing construction on beaches, near rivers, and paved roads.

Liquefaction was identified at 33 sites, expressed as cracking, ejection of water and sand, formation of sand volcanoes with diameters of up to 60 cm, and lateral spreading. Three of these sites were located in the immediate proximity to the epicenter, particularly in the locality of Maruata, while the farthest site from the epicenter was Manzanillo, situated at a distance of 141 km. Liquefaction was primarily observed close to the coastline or along the edges and coastal areas of rivers. Liquefaction primarily affected natural terrain but also extended to structures such as roads, houses and cobblestone squares.

The intensity of these effects, evaluated using the ESI-07 scale, ranged from VII to IX. Approximately six months after the main seismic event, the manifestation of these effects in the natural environment becomes nearly imperceptible. This is primarily because the inhabitants of the affected areas resume normal activities in these places (Fig. 7).

5.2.4. Hydrogeological anomalies

Earthquakes generate physical and chemical alterations in groundwater and surface water (Kissin and Grinevsky, 1990; Muir-Wood and King, 1993; Rojstaczer and Wolf, 1991). The hydrogeological changes can affect the quantity, quality, physico-chemical properties, level, and flow direction of water, and are related to a complex interplay of watershed and aquifer characteristics, geology and seismicity. These hydrogeological variations can create problems for emergency management and the long-term administration of water resources in the affected area (Esposito et al., 2002, Esposito et al., 2009; Binda et al., 2020). Also, this effect can be linked to other secondary effects such as liquefaction, lateral spreading and landslides.

Five sites displaying hydrogeological anomalies have been identified. The site closest to the epicenter exhibits the emergence and disappearance of springs, as well as the drying up of the lagoon in the Motín del Oro locality due to coastal uplift (Fig. 7f). The intensity range for this effect on the ESI-07 I = VII - X.

The hydrogeological anomalies can be observed farther from the epicenter than other EEEs, supporting the suggestion made by e.g., Porfido et al. (2007), that hydrogeological anomalies are the most common EEEs observed in the far field.

5.2.5. Anomalous waves and Tsunami

Coseismic tsunamis are generated when there is a displacement of the seafloor due to surface faulting, or they can be generated by secondary processes (e.g., landslide masses entering a body of water). The dimension of a tsunami depends on multiple factors, including the amount of slip and extension of the rupture plane, the local bathymetry and the morphology of the affected coastal area (Lario et al., 2016; Hill et al., 2024).

Anomalous waves were recorded at six locations, while the national tide gauge service reported tsunami phenomena at 11 sites. The maximum wave amplitude was documented at the Manzanillo station in Colima, reaching 1.745 m (SMN, 2022). However, the effect was observed to the south, at a maximum distance of 2510 km from the epicenter, in the Santa Cruz and Baltra islands of the Galápagos, Ecuador (Miranda et al., 2022). The intensity range for this effect on the ESI-07 I=IV – IX.

5.3. ESI-07 macroseismic fields and epicentral intensity

The assignment of ESI-07 intensity according to the ESI-07 scale guidelines (see Methods, Section 4), is based on the distribution of the EEEs and its fundamental characteristics. The ESI-07 scale offers high spatial resolution, capturing variations in EEEs related to geological and geomorphological conditions, independent of human constructions. The assignment of the intensity values enables us to draw isoseismal maps, which may support seismic hazard assessment (Papathanassiou et al., 2017a, 2017b). Table 2 shows a synthesis of the identified EEE's and their distribution both spatially and in the ESI-07 intensity range. The dataset is made publicly available (see Data Availability section). For points surveyed in the field and collected from online sources, data include an informative sheet for each documented EEE, specifying the type of effect, local setting, a description and photographic documentation. Shapefiles are provided as well. For landslides mapped from satellite images, we provide the polygonal inventory in shapefile format.

Fig. 10 shows the location of the collected EEEs, color-coded according to the ESI-07 intensity. In the first panel a broader region is presented, whereas the second panel focuses on the epicentral region. Landslides mapped remotely are presented as smaller dots to facilitate readability of the map, but taking into consideration its intensity value for the trace of each isoseismal line. ESI-07 isoseismals were drawn, representing the areas that suffered the same level of damage. The highest intensity value for the identified landslides is IX, which is highlighted by the triangle symbol in Fig. 10, in the area corresponding to the intensity IX isoseismal zone. The highest isoseismal (ESI-07 X) is mainly constrained by coastal uplift, covering an area of about 500 km^2 stretched along the coastline. ESI-07 intensity IX is constrained by several types of EEEs (tsunami, slope movements, liquefaction, ground cracks) covering an area of over 6000 km^2. ESI-07 isoseismals X and IX are elongated in a NW-SE direction, consistent with the strike of the seismogenic source, while isoseismals VIII and VII are more rounded.

Beside the ESI-07 intensity attributed to individual sites, an ESI-07 epicentral intensity (I_0) can be estimated based on three different ways of reasoning: i) surface rupture length; ii) amount of permanent ground displacement; iii) dimension of the area affected by secondary effects.

Being a subduction earthquake, no surface faulting was observed for the 2022 Michoacan event. The tectonic uplift observed in the field and from geodesy exceeds 40 cm for a 60 km long coastal segment (Figs. 5 and 10), thus pointing towards ESI-07 I_0 = X. When referring to the dimension of the area affected by secondary effects, we obtain a value of 12,300 km^2. In such an estimate, we did not include isolated points

Table 2
Documented earthquake environmental effects: number of sites, ESI-07 intensity values, distance from the epicenter.

EEE	N° of sites	Min-max epicentral distance (km)	Description max effects	ESI-07 range
Ground deformation	12	7–60	Coastal tectonic uplift 90 cm	X
Landslides and rockfalls	7977	7–388	Volume higher than 10^5 m^3	VI - IX
Liquefaction	33	7–141	Cracking of more than 100 m in length and ejection of water and sand and Fractures up to 30 cm width	VII - IX
Ground cracks	36	7–165	Length 18 m, 30 to 50 cm width, depth 53 cm	VI - X
Hydrogeological anomalies	5	21–2350	Emergence and disappearance of springs and drying up of a lagoon	VII - X
Anomalous waves and tsunami	17	7–2500	Runup 1.745 m	IV - IX

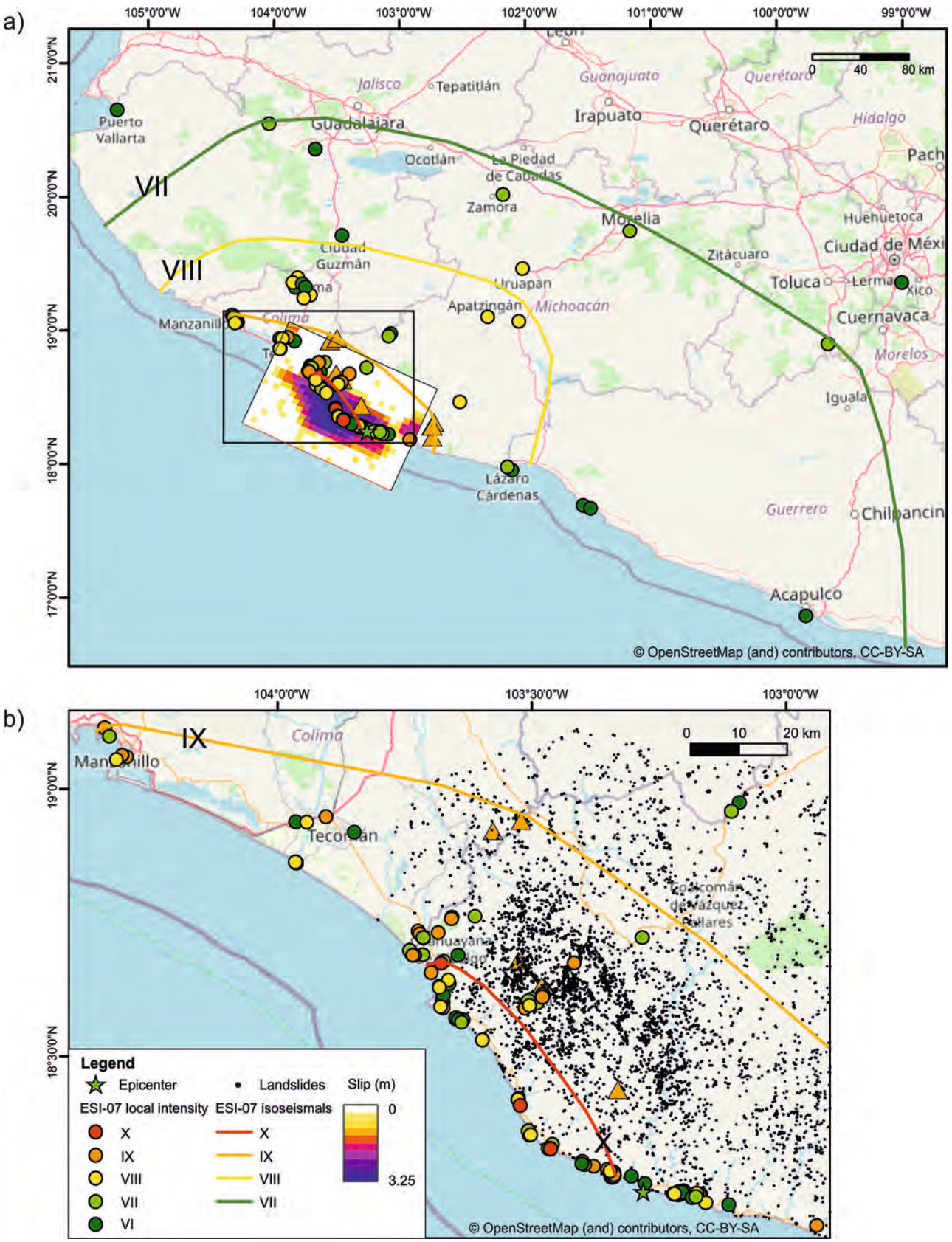

Fig. 10. ESI-07 local intensities and isoseismals for the September 19th, 2022, earthquake. Dots are sites evaluated from field surveys and social media accounts; for the landslides mapped remotely, slope movements with ESI-07 intensity of IX are shown as orange triangles, while all the other smaller movements are shown as black dots. The black rectangle in a) is the area enlarged in panel b). Source model is from USGS, 2022. Basemaps © OpenStreeMap Distributed under the Open Data Commons Open Database License (ODbL) v1.0.

located in the far field, as suggested by Huayong et al. (2019). The obtained value would correspond to ESI I_0 of XI, thus higher than the estimate based on permanent ground deformation; our preferred estimate is $I_0 = X$, as we explain in better detail in the following.

6. Discussion

6.1. Comparison of the Michoacan earthquake with other events analyzed using the ESI-07 scale

The discrepancy in the epicentral intensity values I_0 ESI-07 obtained from different diagnostics (total area affected by EEEs versus amount of coastal uplift) was already observed in large interplate earthquakes along the Pacific Coast of Mexico and Ecuador, specifically in the 2016 Pedernales and 2020 La Crucecita earthquakes (Chunga et al., 2018; Velázquez Bucio et al., 2023a;). Such discrepancy reveals a distinction between earthquakes in coastal subduction zones and those evaluated under the same scale in different geodynamic settings. This makes sense, since, for large subduction earthquakes along the East Pacific Coast the epicentral intensity will be normally underestimated, since the epicenter is typically located offshore. In subduction earthquakes, typically, the offshore impacted area cannot be fully assessed; by definition, macroseismic observations are restricted to onshore areas, and therefore the isoseismals are open towards the sea.

In Fig. 11 we present a comparison among the 2022 Michoacan earthquake and a dataset of over 150 events analyzed with the ESI-07 scale, which demonstrates the reliability of the scale to be applied especially in sparsely populated areas, zone prone to strong earthquakes and in the near field to the epicenter (Ferrario et al., 2022). We focus in particular on the relation among ESI-07 epicentral intensity and moment magnitude or the dimension of the area affected by secondary effects.

From the original database (Ferrario et al., 2022), we extracted the earthquakes occurring along subduction interface zones, depicted as red squares; we also highlighted the 2017 Gulf of Tehuantepec earthquake, which represents the only intraslab event in the dataset. The plots show that there is a direct relation among magnitude, dimension of the affected area and ESI-07 epicentral intensity. This observation is not surprising, but here we stress that subduction zone earthquakes lie on the right side of the plots, meaning that they represent an "end-member" within the dataset. For a given magnitude, subduction earthquakes have a lower ESI-07 epicentral intensity (Fig. 11a). This fact is due to two main reasons. First, subduction earthquakes generally have a deeper hypocentral depth than crustal events (median values in Fig. 11a are 11 km for the entire dataset and 23 km for subduction earthquakes). Second, if the epicenter lies offshore, the macroseismic field is incomplete and epicentral intensity is estimated based on the strongest visible effects, which actually may be located some kilometers or tens of kilometers far from the epicenter. In summary, the discrepancy in epicentral intensity estimates is partly related to the different rate of decrease of primary and secondary effects with respect to distance from the source. Accordingly, one could expect an underestimation of the epicentral intensity for earthquakes with offshore epicenters, consistent with what is shown in Fig. 11. The black dashed line in Fig. 11a represents the empirical equation derived by Ferrario et al. (2022) on the entire dataset; if considering only subduction zone earthquakes, the fitting curve would be steeper (dashed red line in Fig. 11a). Even though it seems something obvious, this difference in the rate of decrease is an important feature to consider when comparing subduction earthquakes with other types of events. These observations prompt the need to derive scaling relations specific for this geodynamic setting.

6.2. Relations between the ESI-07 macroseismic field and satellite geodesy

We recall that the observed vertical displacement also includes a component that occurred after the mainshock, even if based on the interviews with local witnesses most of the vertical displacement occurred coseismically. However, even a qualitative comparison of field observations and available space geodesy information (Liu et al., 2023) shows interesting results.

As already suggested (Papathanassiou et al., 2017a, 2017b; Mavroulis et al., 2021; Naik et al., 2023a, 2023b), the macroseismic intensity estimation might take advantage of space geodesy technology. In the case of the September 19th, 2022, Michoacan earthquake, we observe that coastal uplift significantly correlates with the region of maximum vertical displacement illustrated by C-band Sentinel-1 satellite synthetic aperture radar (SAR) images (Liu et al., 2023; Fig. 5). Likewise, the spatial distribution of coseismic landslides is consistent with the area of maximum deformation derived from both InSAR and GNSS. This indicates that the InSAR data and high-resolution satellite images could provide crucial information on both primary and secondary environmental effects. We argue that field observations are suitably complemented by remote sensing geodetic analyses for developing macroseismic intensity estimation in seismic hazard analysis in the Mexico coastal region, as well as elsewhere in the world.

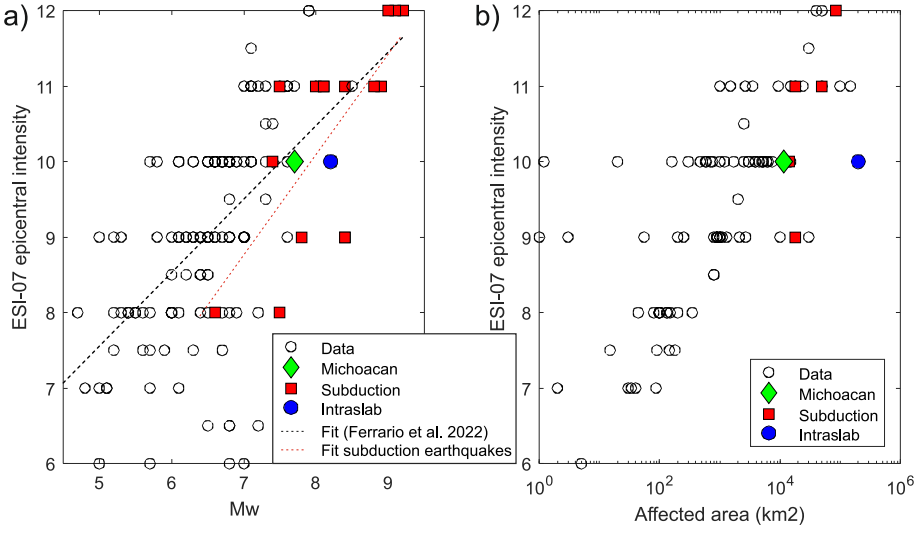

Fig. 11. Graphical comparison of the 2022 Michoacan earthquake with a dataset of global seismic events analyzed using the ESI-07 scale; a) ESI-07 epicentral intensity versus moment magnitude; b) ESI-07 epicentral intensity versus area affected by secondary effects. Subduction earthquakes are highlighted as red squares. Dataset after Ferrario et al., 2022. (For interpretation of the references to color in this figure legend, the reader is referred to the web version of this article.)

6.3. ESI-07 for the seismic hazard and social impact in the Mexican subduction zone

This paper refrains from providing an exhaustive analysis of the intricate societal implications following the 2022 Michoacán earthquake, encompassing psychological, engineering geology and financial dimensions. Nevertheless, our investigations yield some insights that allow for some overarching observations regarding the earthquake's societal impact, primarily within the epicentral zone. Specifically, attention is drawn to two pivotal aspects: firstly, concerning safety and security within the affected region, and secondly, focusing on the earthquake's direct repercussions and the potential for learning from this event to fortify future preparedness.

The most heavily impacted area resides along the Mexican Pacific Coast, particularly in the states of Colima and Michoacán, which present unsafe conditions for residents (U.S. Department of State, 2023). This situation significantly affects fieldwork aimed at collecting information on the earthquake's effects. Security concerns have led to restricted access across large swaths of the epicentral area, resulting in an asymmetrical distribution of observed effects concerning both their proximity to the epicenter and their uneven spatial distribution.

As illustrated in Fig. 3b, the epicentral area is characterized by low population density, excluding major urban clusters like Colima-Villa de Álvarez, Manzanillo, and Tecomán in the Colima State, and Lázaro Cárdenas in the state of Michoacán. Beyond these, most localities have populations below 10,000 inhabitants, with many, particularly in the epicentral area, comprising only a few hundred residents. Moreover, to obtain comprehensive information from an area affected by an earthquake it is essential that the electrical service be operational, and there must be signal and internet connectivity, enabling people to report their experiences. In fact, the comparison of Figs. 3 and 10 highlights the need to integrate evaluations using traditional scales, effective in populated areas with developed infrastructure, with the ESI-07 scale, ideal for documenting seismic effects in sparsely populated areas with limited infrastructure and communication, such as the Pacific coastal strip of Mexico. This integration allows one to obtain a complete record of the effect caused by the earthquake in the territory.

The epicenter is located near the Municipality of Aquila, Michoacán—a region encompassing 418 localities with a total population of 24,676 as per the 2020 Census (INEGI Instituto Nacional de Estadística y Geografía, 2023a)—experienced severe impact, notably affecting Maruata, the third-largest locality of the Municipality, with approximately 1000 inhabitants. Surveys reveal Maruata as one of the worst-hit areas, compounded by the incapacity of the Maruata Community Hospital to render assistance due to significant structural damage.

As described in the Introduction, the region endured the substantial impact from the 1973 Colima Earthquake (M_w 7.6), yet this did not prompt substantial changes in land-use planning or construction regulation. Historically, cyclones/hurricanes posed much more frequent threats than earthquakes, influencing infrastructure design to prioritize resilience against the former. Even if it did not affect the 2022 earthquake epicentral area, the devastating effects on Acapulco of the October 25th, 2023, Hurricane Otis (NASA Earth Observatory, 2023) are a clear reminder of similar extreme natural hazards. Consequently, while wooden structures demonstrate relative resilience to seismic events, the majority of buildings, constructed using masonry or reinforced concrete, exhibit vulnerability to earthquakes. This susceptibility is further exacerbated in areas prone to liquefaction or landslides, leading to potential total destruction of buildings.

Indeed, depending on the physical, geological and climatic conditions of a region, EEEs may trigger cascading effects, either environmental, physical, or social. An example of this can be found in the locality of Motín del Oro, where coastal uplift is associated with the desiccation and emergence of springs and the drying up of a lagoon (Fig. 4a, b) located between the coastal area and the inhabited zone. This lagoon used to be a source of livelihood for the residents, who fished and sold their products. Now that the lagoon has dried up, residents are also discussing land ownership for agricultural purposes. Furthermore, the lagoon served as a natural barrier between domestic animals, such as dogs and pigs, inhabiting the populated area, and the population of sea turtles that come to nest in this locality, considered a sanctuary for three turtle species (Fuentes-Farias et al., 2010). Without the presence of the lagoon as a barrier, domestic animals have become the primary predators of turtle eggs, which could pose ecosystem-level issues. Although this topic is not the central focus of this research, these are aspects that can be considered for the assessment of environmental impacts caused by earthquakes, and mitigation of residual risk (UNISDR, 2009).

Bruneau et al. (2003) extend the concept of resilience to seismic territories, defining it as the capacity of social units to mitigate hazards, manage disaster aftermath, and execute recovery efforts to minimize societal disruptions and future seismic impacts. We express the hope that the 2022 earthquake will motivate the authorities and local communities to strengthen the resilience of the region against future seismic events, thereby curbing economic ramifications and safeguarding human well-being.

7. Conclusions

The use of ESI-07 scale allowed to map in detail the macroseismic intensity in the epicentral area of the September 19th, 2022, megathrust earthquake. This would have been impossible using the "traditional", damage-based intensity scales. In fact, most of the epicentral area is very sparsely populated (Fig. 3). The only documentation available for macroseismic analysis is therefore based on the large impact of this earthquake on the physical environment.

For the first time, the ESI-07 assessment took advantage of more than 8000 sites with environmental effects (publicly available in Velázquez-Bucio et al., 2023b), a number that is one order of magnitude larger than previous case histories available in the literature. This is made possible essentially by the availability of satellite imagery which allows building very accurate landslide inventories.

The 2022 Michoacán earthquake exhibited a tectonic uplift greater than 40 cm along a 60 km coastal segment, indicating an ESI-07 $I_0 = X$, which is our preferred estimate. Considering the dimension of the area affected by secondary effects of 12,300 km^2, the ESI I_0 would be XI. Discrepancies in the values of I_0 ESI-07, observed in several subduction earthquakes (; Velázquez-Bucio et al., 2023a), indicate that this is due to factors such as their greater hypocentral depth and incomplete offshore macroseismic field. Results from the present study and previous large intraplate subduction earthquakes therefore suggest the need to develop specific scaling relationships that fit the particularities of subduction zone earthquakes. When the ESI-07 scale was released, there was no distinction between different geodynamic settings or seismological properties. We argue that today there is a sufficient number of case histories to move towards the consideration of such aspects in the intensity evaluation.

This analysis focused on the evaluation of the EEEs generated by the 2022 Michoacán earthquake through the ESI-07 scale, has also provided insights into the social impact of this type of events in the very wide epicentral area. The lack of basic services, such as electricity, telephone and internet signals, and roads, emphasizes the importance of investigating environmental coseismic effects for an accurate assessment of macroseismic intensity. The vulnerability of buildings to earthquakes secondary hazards is highlighted, especially in areas prone to liquefaction or landslides. In Mexico as in many Latin American countries, such data are particularly important for hazard and risk assessment which too often only considers the primary seismic hazard, through ground acceleration. However, in coastal areas and in mountainous areas of the Mexican Pacific, environmental effects such as liquefaction or landslides could potentially cause more casualties or damage more infrastructure than primary acceleration. These effects must absolutely be taken into

account in risk assessments and must justify the intensification of such studies in the future. Ultimately, this study gives prominence to the need to strengthen resilience in the region against future seismic events, with the aim of reducing economic repercussions and protecting human well-being.

Funding

This work was supported by the Universidad Nacional Autónoma de México (UNAM), Postdoctoral Program (POSDOC), awarded to M.M.V. B., at the Centro de Geociencias (CGeo), UNAM, Juriquilla; PAPIIT grant IN108220 and IG101823 awarded to P.L.; E.M., M.F. F., M.P. and A.M. M. have been funded by the European Union – NextGenerationEU – Mission 4 "Education and Research" – Component 2 "From Research to Business" – Investment 3.1 "Fund for the realization of an integrated system of research and innovation infrastructures" – Project IR0000037 – GeoSciences IR. Partial support was received from the France-Mexico collaborative project SEP-CONACYT-ANUIES-ECOS N° 321193 and the IGCP-669 Ollin Project of UNESCO-IUGS. We also acknowledge the support for academic exchange PAEP-UNAM to A.M.M., and the INQUA Fellowship for Early Career Researcher awarded to M.M.V.B. to attend the XXI INQUA Congress Roma 2023.

CRediT authorship contribution statement

María Magdalena Velázquez-Bucio: Writing – original draft, Project administration, Investigation, Formal analysis. **Maria Francesca Ferrario:** Writing – original draft, Methodology, Investigation, Formal analysis, Conceptualization. **Pierre Lacan:** Writing – review & editing, Supervision, Funding acquisition. **Eliana Muccignato:** Visualization, Resources, Data curation. **Marco Pizza:** Investigation, Data curation. **Aadityan Sridharan:** Resources, Investigation. **Sabina Porfido:** Validation, Investigation. **Sundararaman Gopalan:** Investigation. **Andrés Nuñez-Meneses:** Investigation. **Alessandro Maria Michetti:** Writing – review & editing, Supervision, Formal analysis, Conceptualization.

Declaration of competing interest

The authors declare that they have no conflict of interest.

Data availability

Data in this article are openly available.

Historical seismicity; aftershocks data; September 19th, 2022 Michoacán earthquake data and report are from Servicio Sismológico Nacional (SSN), www.ssn.unam.mx. Tide gauge data are provided by the Servicio Mareográfico Nacional (SMN), http://www.mareografico.unam.mx/portal/ and CICESE: Calendarios de mareas en México, https://predmar.cicese.mx/. ¿Sintió un Sismo? data can be downloaded from the UANL website: http://sismos.uanl.mx/.

Supplement. A description of the documented EEEs and the inventory of mapped landslides (shapefile format) are available at https://zenodo.org/records/10015781

Acknowledgments

We thank Professor Gerardo Leyte (UMAR) for his assistance and comments in the analysis for the interpretation of sea level bioindicator species in coastal surveys; Fernando Monterroso (IREA – CNR) and Simone Atzori (INGV), for the discussion on interferometry analysis and displacement model; and Dr. Juan Carlos Montalvo Arrieta, for providing data from the "¿Sintió un sismo?" program. Special thanks to J. Daniel Guzmán Espinosa (SARMéxicoByS Michoacán coordinator), Eng. Sergio Aguilar Flores, Geophysical Eng. Antonio de J. Mendoza (SSN), Lizbeth Robles Ruíz, Firefighter and Lifeguard SARMéxicoBYS Michoacán, and Leonardo Macías Pineda, Member of the United Nations Organization (ONU), for their collaboration and effort in carrying out the fieldwork, undoubtedly an invaluable contribution. We thank Planet for providing PlanetScope imagery as part of the Education and Research Program. Thanks to Paula J. Noble for her invaluable help with her suggestions and language review. This paper benefited from detailed and constructive review from four anonymous referees, we are grateful for their comments which substantially helped improving the quality of our work.

Appendix A. Supplementary data

Supplementary data to this article can be found online at https://doi.org/10.1016/j.enggeo.2024.107776.

References

Atzori, S., Monterroso, F., Antonioli, A., De Luca, C., Svigkas, N., Casu, F., Manunta, M., Quintiliani, M., Lanari, R., 2023. Automatic seismic source modeling of InSAR displacements. Int. J. Appl. Earth Obs. Geoinf. 123, 103445. https://doi.org/10.1016/j.jag.2023.103445.

Barrios, R.F., Bastida, J.R., Rosales, F.E., 2000. Carta geológico-minera Lázaro Cárdenas, escala 1:250,000, estados de Michoacán, Colima y Guerrero, Consejo de Recursos Minerales, Secretaría de Economía, México, p. 108.

Bhattacharya, S., Hyodo, M., Goda, K., Tazoh, T., Taylor, A., 2011. Liquefaction of soil in the Tokyo Bay area from the 2011 Tohoku (Japan) earthquake. Soil Dyn. Earthq. Eng. 31, 1618–1628. https://doi.org/10.1016/j.soildyn.2011.06.006.

Binda, G., Pozzi, A., Michetti, A.M., Noble, P.J., Rosen, M.R., 2020. Towards the Understanding of Hydrogeochemical Seismic Responses in Karst Aquifers: A Retrospective Meta-Analysis Focused on the Apennines (Italy). Minerals 10, 1058. https://doi.org/10.3390/min10121058.

Bodin, P., Klinger, T., 1986. Coastal uplift and mortality of intertidal organisms caused by the September 1985 Mexico earthquakes. Science 233 (4768), 1071–1073. https://doi.org/10.1126/science.233.4768.1071.

Bruneau, M., Chang, S., Eguchi, R., Lee, G., O'Rourke, T., Reinhorn, A., Shinozuka, M., Tierney, K., Wallace, W., Von Winterfeldt, D., 2003. A framework to quantitatively assess and enhance the seismic resilience of communities. Earthquake Spectra 19, 733–752. https://doi.org/10.1193/1.1623497.

Castilla, J.C., Manríquez, H.M., Camaño, A., 2010. Effects of rocky shore coseismic uplift and the 2010 Chilean mega-earthquake on intertidal biomarker species. Mar. Ecol. Prog. Ser. 418, 17–23. https://doi.org/10.3354/meps08830.

Chen, K., Feng, W., Liu, Z., Song, Y.T., 2018. Mw 8.1 Tehuantepec earthquake: deep slip and rupture directivity enhance ground shaking but weaken the tsunami. Seismol. Res. Lett. 89 (4), 1314–1322. https://doi.org/10.1785/0220170277.

Chen, B., Yu, Z., Li, L., Zheng, R., Wu, C., 2023. Surface deformation and damage of 2022 (M 6.8) Luding earthquake in China and its tectonic implications. Open Geosci. 15 (1), 20220490. https://doi.org/10.1515/geo-2022-0490.

Chunga, K., Livio, F., Mulas, M., Ochoa-Cornejo, F., Besenzon, D., Ferrario, M.F., Michetti, A.M., 2018. Earthquake Ground Effects and Intensity of the 16 April 2016 M w 7.8 Pedernales, Ecuador, earthquake: implications for the source characterization of large subduction earthquakes. Bull. Seismol. Soc. Am. 108 (6), 3384–3397. https://doi.org/10.1785/0120180051.

Chunga-Llauce, J.A., Pacheco, A.S., 2021. Impacts of earthquakes and tsunamis on marine benthic communities: A review. Mar. Environ. Res. 171, 105481. https://doi.org/10.1016/j.marenvres.2021.105481.

CICESE, 2022. Calendarios de mareas en México. https://predmar.cicese.mx/ last access 8 August 2023.

Coastal_uplift_Maruata, 2019. https://sponkoepicuro.wordpress.com/2019/05/12/maruata-michoacan/ last access 15 April, 2023.

CONAGUA, 2020. Actualización de la disponibilidad media anual de agua en el acuífero Ostula (1619). In: Estado de Michoacán. Comisión Nacional del Agua (CONAGUA): Disponibilidad Media Anual por Acuíferos | CONAGUA last access September 28, 2023.

De Mets, C., Wilson, D.S., 1997. Relative motions of the Pacific, Rivera, north American, and Cocos plates since 0.78 Ma. J. Geophys. Res. 102, 2789–2806. https://doi.org/10.1029/96JB03170.

DeMets, C., Gordon, R.G., Argus, D.F., Stein, S., 1994. Effect of recent revisions to the geomagnetic reversal timescale. Geophys. Res. Lett. 21, 2191–2194. https://doi.org/10.1029/94GL02118.

DeMets, C., Gordon, R.G., Argus, D., F., 2010. Geologically current plate motions. Geophys. J. Int. 181 (1), 1–80. https://doi.org/10.1111/j.1365-246X.2009.04491.x.

Dengler, L., McPherson, R., 1993. The 17 August 1991 Honeydew earthquake, North Coast California: a case for revising the Modified Mercalli scale in sparsely populated areas. Bull. Seismol. Soc. Am. 83 (4), 1081–1094. https://doi.org/10.1785/BSSA0830041081.

Esposito, E., Pece, R., Porfido, S., Tranfaglia, G., 2002. Hydrological anomalies connected to earthquakes in southern Apennines (Italy). Nat. Hazards Earth Syst. Sci. 1, 137–144. https://doi.org/10.5194/nhess-1-137-2001.

Esposito, E., Pece, R., Porfido, S., Tranfaglia, G., 2009. Ground effects and hydrological changes in the Southern Apennines (Italy) in response to the 23 July 1930 earthquake (MS=6.7). Nat. Hazards Earth Syst. Sci. 9, 539–550. https://doi.org/10.5194/nhess-9-539-2009.

Fan, X., Scaringi, G., Korup, O., West, A.J., Van Westen, C.J., Tanyas, H., Hovius, N., Hales, T.C., Jibson, R.W., Allstadt, E.A., Zhang, L., Evans, S.G., Xu, C., Li, G., Pei, X., Xu, Q., Huang, R., 2019. Earthquake-induced chains of geologic hazards: patterns, mechanisms, and impacts. Rev. Geophys. 57 (2), 421–503. https://doi.org/10.1029/2018RG000626.

Ferrario, M.F., 2022. Landslides triggered by the 2015 M w 6.0 Sabah (Malaysia) earthquake: inventory and ESI-07 intensity assignment. Nat. Hazards Earth Syst. Sci. 22 (10), 3527–3542. https://doi.org/10.5194/nhess-22-3527-2022.

Ferrario, M.F., Livio, F., Michetti, A.M., 2022. Fifteen years of Environmental Seismic Intensity (ESI-07) scale: Dataset compilation and insights from empirical regressions. Quat. Int. 625, 107–119. https://doi.org/10.1016/j.quaint.2022.04.011.

Figueroa, J., 1974. Sismicidad en Colima, macrosismo del 30 de enero de 1973, Rep. 332, 49, Instituto de Ingenieria, U.N.A.M., México, D.F.

Fuentes-Farias, A.L., Garduño-Monroy, V.H., Gutiérrez-Ospina, G., Pérez-Cruz, L., Meléndez-Herrera, E., Urrutia-Fucugauchi, J., 2010. Reconnaissance study of Colola and Maruata, the nesting beaches of marine turtles along the Michoacan coast in southern Mexico. Geofis. Int. 49-4, 201–212.

González-Partida, E., Torres-Rodríguez, V., 1988. Evolución tectónica de la porción Centro-Occidental de México y su relación con los yacimientos minerales asociados. Geofísica Internacional 27-4, 543–581. https://doi.org/10.22201/igeof.00167169p.1988.27.4.810.

Guerrieri, L., Audemard, F., Azuma, T., Baiocco, F., Baize, S., Blumetti, A.M., Brustia, E., Clague, J., Comerci, V., Esposito, E., Gurpinar, A., Grützner, C., Jin, K., Kim, Y.S., Kopsachilis, V., Lucarini, M., McCalpin, J., Michetti, A.M., Mohammadioun, B., Morner, N.A., Okumura, K., Ota, Y., Papathanassiou, G., Pavlides, S., Pérez López, R., Porfido, S., Reicherter, K., Rodríguez Pascua, M.A., Roghozin, E., Scaramella, A., Serva, L., Silva, P.G., Sintubin, M., Tatevosssian, R., Vittori, E., 2015. Earthquake environmental effects for seismic hazard assessment: the ESI intensity scale and the EEE catalogue, 182 p, 97. ISPRA, Rome, Italy. https://doi.org/10.13140/RG.2.1.3629.3202, 978-88-9311-007-5.

Guzzetti, F., Ardizzone, F., Cardinali, M., Rossi, M., Valigi, D., 2009. Landslide volumes and landslide mobilization rates in Umbria, Central Italy. Earth Planet. Sc. Lett. 279, 222–229. https://doi.org/10.1016/j.epsl.2009.01.005.

Hill, E.M., McCaughey, J.W., Switzer, A.D., Lallemant, D., Wang, Y., Sathiakumar, S., 2024. Human amplification of secondary earthquake hazards through environmental modifications. Nat. Rev. Earth Environ 2024, 1–14. https://doi.org/10.1038/s43017-024-00551-z.

Huayong, N., Hua, G., Yanchao, G., Blumetti, A., Comerci, V., Di Manna, P., Guerrieri, L., Vittori, E., 2019. Comparison of Earthquake Environmental Effects and ESI intensities for recent seismic events in different tectonic settings: Sichuan (SW China) and Central Apennines (Italy). Eng. Geol. 258, 105149. https://doi.org/10.1016/j.enggeo.2019.105149.

Imamura, F., Boret, S.P., Suppasri, A., Muhari, A., 2019. Recent occurrences of serious tsunami damage and the future challenges of tsunami disaster risk reduction. Prog. Disaster Sci. 1, 100009. https://doi.org/10.1016/j.pdisas.2019.100009.

INEGI (Instituto Nacional de Estadística y Geografía), 2010. Compendio de información geográfica Municipal de los Estados Unidos Mexicanos. Aquila, Michoacán de Ocampo.

INEGI (Instituto Nacional de Estadística y Geografía), 2023a. Censo de Población y Vivienda: Censo de Población y Vivienda 2020 (inegi.org.mx), last access 13 September 2023..

Jibson, R.W., Tanyaş, H., 2020. The influence of frequency and duration of seismic ground motion on the size of triggered landslides—A regional view. Eng. Geol. 273, 105671. https://doi.org/10.1016/j.enggeo.2020.105671.

King, T.R., Quigley, M., Clark, D., 2018. Earthquake environmental effects produced by the Mw 6.1, 20th May 2016 Petermann earthquake, Australia. Tectonophysics 747–748, 357–372. https://doi.org/10.1016/j.tecto.2018.10.010.

Kissin, I.G., Grinevsky, A.O., 1990. Main features of hydrogeodynamic earthquake precursors. Tectonophysics 178 (2–4), 277–286. ISSN 0040–1951. https://doi.org/10.1016/0040-1951(90)90154-Z.

Lario, J., Bardají, T., Silva, P.G., Zazo, C., Goy, J.L., 2016. Improving the coastal record of tsunamis in the ESI-07 scale: Tsunami Environmental Effects Scale (TEE-16 scale). Geologica Acta: an international earth science journal, vol. 14 (2), 179–193. https://doi.org/10.1344/GeologicaActa2016.14.2.6.

Larsen, I.J., Montgomery, D.R., Korup, O., 2010. Landslide erosion controlled by hillslope material. Nat. Geosci. 3, 247–251. https://doi.org/10.1038/ngeo776.

Linnaeus, C., 1758. Systema naturae, vol. 1. Stockholm, Laurentii Salvii, p. 824.

Liu, C., Lay, T., Bai, Y., He, P., Xiong, X., 2023. Coseismic Slip Model of the 19 September 2022 Mw 7.6 Michoacán, Mexico, earthquake: A Quasi-repeat of the 1973 Mw 7.6 Rupture. Seismic Record. 3 (2), 57–68. https://doi.org/10.1785/0320220042.

Luciérnaga_Noticias, 2022. https://www.facebook.com/luciernaganoticias/posts/pfbid08r1vk8xp7Jxwm48c7Dk5XqGnqWmGZYjgBbVLFkBPq5XfPVEjNsz9RTHjjB5ks5JKl last access 17 October 2022.

Malamud, B.D., Turcotte, D.L., Guzzetti, F., Reichenbach, P., 2004. Landslides, earthquakes, and erosion. Earth Planet. Sc. Lett. 229, 45–59. https://doi.org/10.1016/j.epsl.2004.10.018.

Mavroulis, S., Triantafyllou, I., Karavias, A., Gogou, M., Katsetsiadou, K.-N., Lekkas, E., Papadopoulos, G.A., Parcharidis, I., 2021. Primary and Secondary Environmental Effects Triggered by the 30 October 2020, Mw = 7.0, Samos (Eastern Aegean Sea, Greece) Earthquake Based on Post-Event Field Surveys and InSAR Analysis. Appl. Sci. 11, 3281. https://doi.org/10.3390/app11073281.

Melgar, D., Ruiz-Angulo, A., Pérez-Campos, X., Crowell, B.W., Xu, X., Cabral-Cano, E., Brudzinsky, M.R., Rodríguez-Abreu, R., 2020. Energetic rupture and tsunamigenesis during the 2020 Mw 7.4 La Crucecita, Mexico earthquake. Seimol. Res. Lett. XX, 1–11. https://doi.org/10.1785/0220200272.

Michetti, A.M., Esposito, E., Gürpinar, A., Mohammadioun, B., Mohammadioun, G., Porfido, S., Roghozin, E., Serva, L., Tatevossian, R., Vittori, E., Audemard, F., Comerci, V., Marco, S., McCalpin, J., Mörner, N.A., 2004. The INQUA Scale. An innovative approach for assessing earthquake intensities based on seismically-induced ground effects in natural environment. In: Memorie Descrittive della Carta Geologica d'Italia, Special Volume 67 (ed. Vittori E., and Comerci V.). APAT, Rome, pp. 1–118, 2004.

Michetti, A.M., Esposito, E., Guerrieri, L., Porfido, S., Serva, L., Tatevossian, R., Vittori, E., Audemard, F., Azuma, T., Clague, J., Comerci, V., Gürpinar, A., McCalpin, J., Mohammadioun, B., Morner, N.A., Ota, Y., Roghozin, E., 2007. Environmental seismic intensity scale 2007 - ESI 2007, Mem. Descr.lla Carta Geol. Italia 74, 7–54, Servizio Geologico d'Italia – Dipartimento Difesa del Suolo. APAT, Roma, Italy. http://www.isprambiente.gov.it/en/publications/technical-periodicals/descriptive-memories-of-the-geological-map-of/intensity-scale-esi-2007?set_language=en.

Miranda, E., Abuchar, V., Alcocer, S., Aldea, S., Álvarez, J., Archbold, J., Arroyo, O., Arteta, C., Ballinas, E., Benavides, D., Blandón, C., Bravo, M., Caballero, J., Carrillo, J., Cruz, C., Espinoza, U., Gil, P., Guerrero, H., Gunay, S., Heresi, P., Lubin, C., Mayoral, J., Miranda, S., Pájaro, C., Piscal, C., Rivera, J., Rodríguez, V., Urango, A., Vargas, J., Velasco, L., 2022. Preliminary virtual reconnaissance report (PVRR), in Aquila, Michoacán, Mexico September 19, 2022, Mw 7.6 earthquake, EERI-SMIS Report, DesignSafe-CI. https://doi.org/10.17603/ds2-sbcj-nx44.

Montalvo-Arrieta, J.C., Sosa-Ramírez, R.L., Pérez-Campos, X., 2017. Evaluation of macroseismic intensities in Mexico from recent earthquakes using ¿Sintió un sismo? (did you feel it?). Geofis. Int. 2017 (56–1), 27–36. https://doi.org/10.22201/igeof.00167169p.2017.56.1.1732.

Muir-Wood, R., King, G.C.P., 1993. Hydrological signatures of earthquake strain. J. Geophys. Res. 98 (B12), 035–068. https://doi.org/10.1029/93JB02219.

Naik, S.P., Mohanty, A., Mittal, H., Porfido, S., Michetti, A.M., Yang, B.M., Gwon, O., Kim, Y.S., 2023a. The earthquake environmental effects (EEEs) of the 6th February 2018, Hualien earthquake (Mw=6.4): A contribution to the seismic hazard estimation in the epicentral area. Quat. Int. 656, 48–69. https://doi.org/10.1016/j.quaint.2022.10.009.

Naik, S.P., Mohanty, A., Sotiris, V., Mittal, H., Porfido, S., Michetti, A.M., Gwon, O., Park, K., Jaya, A., Paulik, R., Li, C., Mikami, T., Kim, Y.S., 2023b. Mw 7.5 Sulawesi Supershear Earthquake, Indonesia: Ground effects and macroseismic intensity estimation using ESI-2007 scale. Eng. Geol. 317, 107054. https://doi.org/10.1016/j.enggeo.2023.107054.

NASA Earth Observatory, 2023. Acapulco After Hurricane Otis. https://earthobservatory.nasa.gov/images/152028/acapulco-after-hurricane-otis last access November 29, 2023.

Ordaz, M., Reyes, C., 1999. Earthquake hazard in Mexico City: observations versus computations. Bull. Seismol. Soc. Am. 89, 1379–1383. https://doi.org/10.1785/BSSA0890051379.

Ortlieb, L., Barrientos, S., Guzman, N., 1996. Coseismic coastal uplift and coralline algae record in northern Chile: the 1995 Antofagasta earthquake case. Quat. Sci. Rev. 15 (8–9), 949–960. https://doi.org/10.1016/S0277-3791(96)00056-X.

Papathanassiou, G., Valkaniotis, S., Ganas, A., 2017a. Evaluation of the macroseismic intensities triggered by the January/February 2014 Cephalonia, (Greece) earthquakes based on ESI-07 scale and their comparison to 1867 historical event. Quat. Int. 451, 234–247. https://doi.org/10.1016/j.quaint.2016.09.039.

Papathanassiou, G., Valkaniotis, S., Ganas, A., Grendas, N., Kollia, E., 2017b. The November 17th, 2015 Lefkada (Greece) strike-slip earthquake: Field mapping of generated failures and assessment of macroseismic intensity ESI-07. Eng. Geol. 220, 13–30. https://doi.org/10.1016/j.enggeo.2017.01.019.

Papathanassiou, G., Valkaniotis, S., Ganas, A., Stampolidis, A., Rapti, D., Caputo, R., 2022. Floodplain evolution and its influence on liquefaction clustering: the case study of March 2021 Thessaly, Greece, seismic sequence. Eng. Geol. 298, 106542. https://doi.org/10.1016/j.enggeo.2022.106542.

Pardo, M., Suárez, G., 1995. Shape of the subducted Rivera and Cocos plates in southern Mexico, seismic and tectonic implications. J. Geophys. Res. 100, 12357–12373. https://doi.org/10.1029/95JB00919.

Pérez-Campos, X., Espíndola, V.H., Pérez, J., Estrada, J.A., Cárdenas Monroy, C., Bello, D., González-López, D., González Ávila, D., Contreras Ruiz Esparza, M.G., Maldonado, R., Tan, Y., Rodríguez Rasilla, I., Vela Rosas, M.A., Cruz, J.L., Cárdenas, A., Navarro Estrada, F., Hurtado, A., Mendoza Carvajal, A.J., Montoya-Quintanar, E., Pérez-Velázquez, M.A., 2018. The Mexican National Seismological Service: an Overview. Seismol. Res. Lett. 89 (2A), 318–323. https://doi.org/10.1785/0220170186.

Playa_Motín_Del_Oro_Michoacán, 2020. https://www.facebook.com/photo?fbid=909153766147155&set=pcb.909154139480451&locale=es_ES last access 12 April 2023.

Porfido, S., Esposito, E., Vittori, E., Tranfaglia, G., Guerrieri, L., Pece, R., 2007. Seismically induced ground effects of the 1805, 1930 and 1980 earthquakes in the Southern Apennines, Italy. Ital. J. Geosci. 126 (2), 333–346.

Porfido, S., Alessio, G., Gaudiosi, G., Nappi, R., 2020. New perspectives in the definition/evaluation of seismic hazard through analysis of the environmental effects induced by earthquakes. Geosciences 10, 58. https://doi.org/10.3390/books978-3-0365-1878-7. MDPI.

INEGI (Instituto Nacional de Estadística y Geografía), 2023b. Procesamiento de datos GNSS considerando deformaciones del Marco Geodésico en el tiempo / Instituto Nacional de Estadística y Geografía, México, 28 p. https://www.inegi.org.mx/app/biblioteca/ficha.html?upc=889463912811.

Reyes, A., Brune, J.N., Lomnitz, C., 1979. Source mechanism and aftershock study of the Colima, Mexico earthquake of January 30, 1973. Bull. Seismol. Soc. Am. 69 (6), 1819–1840. https://doi.org/10.1785/BSSA0690061819.

Rojstaczer, S., Wolf, S., 1991. Hydrologic changes Associated with the Loma Prieta Earthquake in the San Lorenzo and Pescadero Drainage Basins. U.S. Geological Survey 91-567. https://doi.org/10.3133/ofr91567.

Rose, A., McKee, J., Sims, K., Bright, E., Reith, A., Urban, M., 2023. LandScan Global 2019, Oak Ridge National Laboratory [Data set]. https://doi.org/10.48690/1524214.

Ruff, L.J., Miller, A.D., 1994. Rupture process of large earthquakes in the northern Mexico subduction zone. Pure Appl. Geophys. 142, 101–172. https://doi.org/10.1007/BF00875970.

Santoyo, M.A., Mikumo, T., Quintanar, L., 2006. Faulting process and coseismic stress change during the 30 January, 1973, Colima, Mexico interplate earthquake (Mw= 7.6). Geofis. Int. 45 (3), 163–178. https://doi.org/10.22201/igeof.00167169p.2006.45.3.203.

Sawires, R., Santoyo, M.A., Peláez, J.A., Henares, J., 2021. Western Mexico seismic source model for the seismic hazard assessment of the Jalisco-Colima-Michoacán region. Nat. Hazards 105 (3), 2819–2867. https://doi.org/10.1007/s11069-020-04426-6.

Serva, L., Vittori, E., Comerci, V., Esposito, E., Guerrieri, L., Michetti, A.M., Mohammadioun, B., Mohammadioun, G.C., Porfido, S., Tatevossian, R.E., 2016. Earthquake hazard and the environmental seismic intensity (ESI) scale. Pure Appl. Geophys. 173 (5), 1479–1515. https://doi.org/10.1007/s00024-015-1177-8.

Singh, S.K., Pardo, M., 1993. Geometry of the Benioff zone and state of stress in the overriding plate in Central Mexico. Geophys. Res. Lett. 20, 1483–1486. https://doi.org/10.1029/93GL01310.

Singh, S.K., Iglesias, A., Arroyo, D., Pérez-Campos, X., Ordaz, M., Mendoza, C., Corona-Fernández, R.D., River, A.L., Espíndola, V.H., González-Ávila, D., Martínez-López, R., Castro-Artola, O., Santoyo, M.A., Franco, S.I., 2023a. A Seismological Study of the Michoacán-Colima, Mexico, earthquake of 19 September 2022 (Mw7.6). Geofis. Int. 62-2, 445–465. https://doi.org/10.22201/igeof.2954436xe.2023.62.2.1453.

Singh, S.K., Corona-Fernandez, R.D., Santoyo, M.Á., Iglesias, A., 2023b. Repeating large Earthquakes along the Mexican Subduction Zone. Seismol. Res. Lett. XX, 1–21. https://doi.org/10.1785/0220230243.

SMN, 2022. Reporte rápido: Registro en las estaciones del Servicio Mareográfico Nacional del tsunami producido por el sismo de magnitud 7.7 ocurrido en Michoacán, Grupo de Trabajo del Servicio Mareográfico Nacional, Instituto de Geofísica, Universidad Nacional Autónoma de México, 15 pp. https://chalchiuhtlicue.geofisica.unam.mx/wp-content/uploads/2022/09/2022-09-19_ReporteRapidoTsunamiMichoacan.pdf.

SSN, 2022. Reporte especial: Sismos del 19 de septiembre de 2022, Michoacán (M7.7). Servicio Sismológico Nacional. IGEF - UNAM. México, 10 pp. http://www.ssn.unam.mx/sismicidad/reportes-especiales/2022/SSNMX_rep_esp_20220919_Michoacan_M74.pdf.

SSN, 2023. Servicio Sismológico Nacional, Instituto de Geofísica, Universidad Nacional Autónoma de México, México. http://www.ssn.unam.mx/sismos-fuertes/. Last access 27 July, 2023.

Suárez, G., Albini, P., 2009. Evidence for great tsunamigenic earthquakes (M 8.6) along the Mexican subduction zone. Bull. Seismol. Soc. Am. 99 (2A), 892–896. https://doi.org/10.1785/0120080201.

Suárez, G., Novelo-Casanova, D.A., 2018. A pioneering aftershock study of the destructive 4 January 1920 Jalapa, Mexico, earthquake. Seismol. Res. Lett. 89 (5), 1894–1899. https://doi.org/10.1785/0220180150.

Suárez, G., Ruiz-Baron, D., Chico-Hernández, C., Zúñiga, F.R., 2020. Catalog of preinstrumental earthquakes in Central Mexico: epicentral and magnitude estimations based on macroseismic data. Bull. Seismol. Soc. Am. XX, 1–16. https://doi.org/10.1785/0120200127.

Suter, M., 2019. The 1563 MI 8 Puerto de la Navidad subduction-zone and 1567 M w 7.2 Ameca crustal earthquakes (western Mexico): New insights from sixteenth-century sources. Seismol. Res. Lett. 90 (1), 366–375. https://doi.org/10.1785/0220180304.

Suter, M., Carrillo-Martínez, M., Quintero-Legoretta, O., 1996. Macroseismic study of shallow earthquakes in the central and eastern parts of the trans-Mexican volcanic belt, Mexico. Bull. Seismol. Soc. Am. 86, 1952–1963. https://doi.org/10.1785/BSSA0860061952.

Tanyas, H., Lombardo, L., 2020. Completeness index for Earthquake-Induced landslide inventories. Eng. Geol. 264, 105331. https://doi.org/10.1016/j.enggeo.2019.105331.

Tanyas, H., Allstadt, K.E., Van Westen, C.J., 2018. An updated method for estimating landslide-event magnitude. Earth Surf. Process. Landf. 43 (9), 1836–1847. https://doi.org/10.1002/esp.4359.

U.S. Department of State, 2023. Travel.State.Gov. https://travel.state.gov/content/travel.html.

UNISDR, 2009. UNISDR Terminology on Disaster Risk Reduction, United Nations International Strategy for Disaster Reduction, Geneva, Switzerland (2009), 30 pp. http://www.undrr.org/quick/10973.

USGS, 2022. https://earthquake.usgs.gov/earthquakes/eventpage/us7000i9bw/executive last access 13 September, 2023.

Van der Eeckhaut, M., Poesen, J., Govers, G., Verstraeten, G., Demoulin, A., 2007. Characteristics of the size distribution of recent and historical landslides in a populated hilly region. Earth Planet. Sci. Lett. 256 (2007), 588–603. https://doi.org/10.1016/j.epsl.2007.01.040.

Velázquez Bucio, M.M., Ferrario, M.F., Lacan, P., Muccignato, E., Pizza, M., Sridharan, A., Porfido, S., Gopalan, S., Nuñez-Meneses, A., Michetti, A.M., 2023b. Environmental Effects Caused by the Mw 7.7, September 19, 2022, Michoacán (Mexico) (1.0), Zenodo [Data set]. https://doi.org/10.5281/zenodo.10015781.

Velázquez-Bucio, M.M., Ferrario, M.F., Muccignato, E., Porfido, S., Sridharan, A., Chunga, K., Livio, F., Gopalan, S., Michetti, A.M., 2023a. Environmental effects caused by the Mw 8.2, September 8, 2017, and Mw 7.4, June 23, 2020, Chiapas-Oaxaca (Mexico) subduction events: comparison of large intraslab and interface earthquakes. Quat. Int. 651, 62–76. https://doi.org/10.1016/j.quaint.2021.11.028.

Verdugo, R., González, J., 2015. Liquefaction-induced ground damages during the 2010 Chile earthquake, Soil Dynamics and Earthquake Engineering. B 79, 280–295. https://doi.org/10.1016/j.soildyn.2015.04.016.

Wirth, E.A., Sahakian, V.J., Wallace, L.M., Melnick, D., 2022. The occurrence and hazards of great subduction zone earthquakes. Nat. Rev. Earth Environ. 3 (2), 125–140. https://doi.org/10.1038/s43017-021-00245-w.

Xu, C., Xu, X., Shen, L., Yao, Q., Tan, X., Kang, W., Ma, S., Wu, X., Cai, J., Gao, M., Li, K., 2016. Optimized volume models of earthquake-triggered landslides. Sci. Rep. 6, 29797. https://doi.org/10.1038/srep29797.

Zúñiga, F.R., Suárez, G., Figueroa-Soto, Á., Mendoza, A., 2017. A first-order seismotectonic regionalization of Mexico for seismic hazard and risk estimation. J. Seismol. 21, 1295–1322. https://doi.org/10.1007/s10950-017-9666-0.